Applied Ocean Research 148 (2024) 104015

Contents lists available at ScienceDirect

Applied Ocean Research

journal homepage: www.elsevier.com/locate/apor

Spatial energy evolution of focused waves generated in numerical wave tank

Guochun Xu [a], Yan Zhou [b,*], Shiqiang Yan [c], Shuai Yuan [a]

[a] Faculty of Maritime and Transportation, Ningbo University, Ningbo, Zhejiang, China
[b] School of Engineering, University of Liverpool, Liverpool, UK
[c] School of Engineering and Mathematical Sciences, City University of London, London, UK

ARTICLE INFO

Keywords:
Focused wave generation
Energy evolution
Wave amplitude spectrum

ABSTRACT

This paper numerically investigates the energy evolution of the focused wave and its correlation with input parameters for the wave generation. The focused wave is numerically generated based on the fully nonlinear potential wave theory which is solved by the Quasi Arbitrary Lagrangian Eulerian-Finite Element Method. The investigation is performed by dividing the generated wave energy into three categories according to their frequency intervals, i.e., the initially assigned frequency interval $[\mathbf{f_1}\ \mathbf{f_N}]$, the frequencies lower ($\mathbf{f} < \mathbf{f_1}$) and higher ($\mathbf{f} > \mathbf{f_N}$) than the initial interval. The amount of the generated energy falling into three energy categories and the energy distribution in the initial frequency interval are analysed against amplitude parameters and frequency bands under three amplitude spectra. Four indicators are proposed to indicate the actual energy variations comparing to the initial design. It is found that for all the three frequency intervals the energies increase when the amplitude parameters increases or the given frequency shifts towards the lower frequency domain. The choice of wave amplitude spectrum plays a significant role to maintain the distribution of the energy in the design frequency range and to minimise the energies out of the design frequency range. The results from the second-order wave group theory are used to assist analyses of the mechanism of the energy evolution alongside the focused wave generation. It is found that the lower-frequency energy in the vicinity of the focusing point is dominated by the second-order difference waves, whereas the higher-frequency energy is mainly produced by the wave flap. The waves which are higher than the second-order and the complex interactions not considered by the second-order wave theory are found significantly disturbing the energy distribution in the originally assigned wave-frequency interval.

1. Introduction

Focused waves simulated by either physical or numerical wave tanks are often selected as representative wave states and have been applied to many studies associated with naval architecture and ocean engineering. The earliest application is to evaluate the seaworthiness characteristics of ships under focused waves by laboratory model tests (Takezawa and Hirayama, 1976). Accurate focused wave packet as designed energy spectra enable effective estimation of the response amplitude operators (RAOs) of ships by a single test, which is more efficient than commonly-adopted measurements from multiple regular waves. To accurately obtain RAOs, the focused wave energy and its distribution over the specified frequency interval should be properly designed and they are expected to be maintained in the wave generation process, to avoid nonlinear responses such as ringing (Davies et al., 1994) or springing (Riesner and El Moctar, 2021) excited by extra energies produced out of the specified frequency range. As focused waves can be generated with high crest elevations, recently they are often considered as extreme waves for offshore structures design, such as wave energy converters, offshore wind turbines, coastal bridges, etc (van Rij et al., 2021, Rameeza et al., 2020, Rameeza and Ranjan, 2021, Jin et al., 2019, Clauss, 2005, Bai et al., 2021). For such extreme waves, the extra higher-frequency wave energy may lead to failure of the generation due to unexpected wave breaking (Abroug et al., 2020) as the higher frequency energy produced out of the design range contributes to even steeper wave crest elevation.

Focused waves are commonly generated experimentally or numerically based on two types of mechanisms. One is the wave instability

* Corresponding author.
E-mail address: yan.zhou@liverpool.ac.uk (Y. Zhou).

https://doi.org/10.1016/j.apor.2024.104015
Received 21 November 2023; Received in revised form 15 February 2024; Accepted 15 April 2024
Available online 24 April 2024

mechanism or so-called nonlinear self-focusing (Zhang et al., 2019), which assumes that waves have unstable crest or trough elevations as the waves propagate in the wave tank. When meeting certain conditions e.g., BFI > 1 (BFI, i.e., Benjamin-Feir Index, which is the ratio between the wave steepness and the spectral bandwidth, is widely used to evaluate the instability of a wave group) as given in (Onorato et al., 2006), wave energy can quickly focus on side waves, leading to the occurrence of extraordinary high waves. The Schrödinger equation with different nonlinear levels is commonly used to theoretically analyze this generation mechanism. So far, several breather solutions, like Kuznetsov–Ma solution, Akhmediev breather, and the Peregrine solution, have been derived and adopted to simulate extreme waves for investigating responses of ships (Chabchoub et al., 2014, Onorato et al., 2013, Onorato et al., 2013). However, these breather solutions are only valid for producing focused waves with single frequency but not for those with multiple frequencies as they cannot consider interactions among wave components (Abroug et al., 2020) or energy dissipation (Tian et al., 2011). The other mechanism is to generate focused waves by the spatial-temporal focusing of the wave energy. It can be achieved by the dispersion method (Touboul et al., 2006) and the phase modulation method (Baldock et al., 1996). The former generates wave components in decreasing order of frequency, i.e., starting with the component having the highest frequency and ending with one having the lowest frequency. The reflecting wave problem can be easily dealt with, but the smooth transient of each 'chirp' pulse at the beginning of the wave maker movement has to be implemented empirically (Rapp and Melville, 1990). Furthermore, the strong nonlinear interaction among wave components may occur and influence focused wave generation (Tian et al., 2011). The latter is to modulate phases of wave components to make the amplitude of each component arrive at the assigned location and time to achieve focused wave crest. Due to the fact that all the wave components are produced concurrently by the wave maker, the total simulation or testing time will be restricted by the reflection of the low frequency components. Different from the dispersion method, the wave maker motion signal in the phase modulation method can be easily determined and processed to meet the requirements of the wave generation. The phase modulation method can be divided into the single wave train model (Baldock et al., 1996), the double wave model (Deng et al., 2015), the triple wave model (Deng et al., 2015), and the New-Wave model (Whittaker et al., 2018). They have different wave energy allocations of the given wave trains by assigning tailored distributions of amplitudes of wave components (Xu et al., 2019). Considering the wide range of amplitude spectra types and the straightforward implementation of the signal at the wave maker, the phase modulation method is often preferred by researchers to generate focused waves used in hydrodynamic studies.

Regardless of the above mentioned advantages of the phase modulation method, the generated focused waves often differ from the tailored ones due to the wave energy spatio-temporal diffusion, transfer among wave components or spreading over frequency domain in the wave evolution. To restrict wave energy diffusion in space and time, the phase iteration scheme was usually employed to enforce phases of all wave components to reach $\pi/2$ at the specified location and time in the wave basin (Chaplin, 1996, Clauss et al., 2006). On the top of the phase iteration, an iterating modification was further applied to the assigned wave component amplitudes for modifying wave energy transfer among wave components (Schmittner et al., 2009) in wave generations. The wave energy spreading over the frequency domain will produce undesired wave components which cannot be predicted by the linear wave theory (Dean and Dalrymple, 1991). For overcoming those undesired energy alteration in wave generation and to acquire designed focused wave, Khait and Shemer (Khait and Shemer, 2018) decomposed wave surface into free and bound components based on the spatial Zakharov equation, whereas Ma et al. (2022) reversed the target wave surface to the paddle of wave maker. These attempts imply that when the initial energy is properly designed based on focused wave energy evolution characteristics, the tailored focused wave can be effectively generated. However, how the initially given energy links to the final energy distribution of the focused wave is still not fully understood.

The energy evolution of the focused wave in the wave tank is directly associated with the initially assigned wave properties, such as wave crest, focusing position and time, frequency range, and the choice of the wave amplitude spectrum. When a larger crest elevation is assigned, the produced crest elevation is obviously enlarged compared to the input value and actual focusing position is shifted downwards (Baldock et al., 1996, Ai et al., 2014), which means that the actual wave energy increases and spatio-temporally diffuses in the generation process. The focusing position and time were investigated by Xu et al (Xu et al., 2019), suggesting that for a fixed focusing position, only when the focusing time goes beyond a threshold, the focused wave can be generated. It could be inferred that the position and time parameters affect focused wave energy evolution in a combined way. Narrowing frequency range generally leads to a higher crest elevation and maintains the focusing position (Li and Liu, 2015), whereas shifting the frequency range forward with constant bandwidth can maintain the wave crest elevation but move the focusing position backward (Liu, 2021). Those findings indicate that the initially assigned frequency range affects the spatio-temporal diffusion of focused wave energy. Moreover, Xu et al. (2022) compared focused waves produced by wave amplitude spectra with different distributions and found that the one with steeper slope results in larger focusing amplitude at the farther position. The generated focused waves under various assigned parameters suggest that they affect wave energy evolution in the wave tank but further quantitative analyses of the relationship between the generated energy distribution and the initial designed wave properties need to be carried out.

Apart from investigations of the wave energy in terms of the crest elevation and focusing position, direct investigations of the energy evolutions of the focused waves have also been carried out. Tian et al. (2011) divided the energy spectrum into four parts, i.e., the lower frequency region ($\mathbf{f/f_p}$= 0.5–0.9, where f_p is the spectrum peak frequency), the peak region ($\mathbf{f/f_p}$=0.9–1.2), the above-peak region ($\mathbf{f/f_p}$=1.2–1.5) and the higher-frequency region ($\mathbf{f/f_p}$=1.5–2.5). It was observed that increase of the higher-frequency energy was caused by the energy transfer from the above-peak region and the process was reversible in the defocusing process. It was also pointed out that the above-peak energy transfer was noticeable for waves with very high steepness (Abroug et al., 2020), whereas the energies in the above-peak and higher-frequency regions showed periodic spatial variations but that in peak region did not show obvious fluctuation (Ning et al., 2022). Rapp and Melville (1990) used different classification for the energy which is allocated at three frequency intervals, i.e., the initially assigned frequency range, the higher frequency range (over the upper limit of the assigned interval) and the lower one (below the assigned lower limit). They found that as the focused wave packet evolved to the focal position, the assigned wave spectrum significantly lost its shape and the energy at the assigned frequency range was leaked to either higher frequency or lower frequency interval. Baldock et al. (1996) further demonstrated that the amount of energy transferred from the assigned frequency interval to the higher frequency harmonics was more obvious for the cases with larger wave crest elevation. As the higher frequency energy will lead to wave breaking prematurely and affects the maximum wave height (Abroug et al., 2020, Xu et al., 2022), it is important to minimize the higher frequency energy to avoid breaking. When examining the offshore structure responses under focused waves, the lower frequency energy can induce low-frequency drift responses (Xu, 2016), whereas the higher frequency energy may excite nonlinear resonance responses as ringing (Davies et al., 1994, Riesner and El Moctar, 2021). So, to successfully obtain the tailored extreme waves with assigned energy spectra or to accurately test RAOs of the floating structures, the energies at lower or higher frequency have to be carefully evaluated and the energy distribution at initially assigned frequency range has to be

properly designed so as to keep the wave energy as designed. As far as the authors are aware, there are few quantitative studies on the generation of the lower and higher frequency energies or the alternation of the energy distribution at the assigned frequency range.

The energy variations in focused wave generation, especially for the alteration of wave energy distribution from the initially assigned frequency range will be investigated in this study. Firstly, focused waves under different amplitude spectra are generated in the numerical wave tank based on fully nonlinear potential theory (FNPT), solved by the Quasi Arbitrary Lagrangian-Eulerian-Finite Element Method (QALE-FEM). Then the focused wave energy is divided into three categories including the initially assigned frequency interval and the corresponding higher and lower frequency intervals. For the generated focused waves, four indicators are proposed to quantify the energy in the three frequency intervals and the spectrum alternation in the given wave frequency interval. Together with the second-order wave theory, the fully nonlinear results of the spatial variations of the energy accompanying the focused wave evolution are quantitatively analyzed which helps to acquire new insights of the focused wave generation in terms of the temporal and spatial energy variation, so as to better generate tailored focused waves.

This paper is organized as follows. Section 2 outlined the wave theory and the corresponding numerical method employed in the numerical wave tank. The generation principles of focused waves are introduced in Section 3, along with the demonstration of the validation of the numerical wave tank based on experimental data. In section 4, four indicators for describing focused wave energy evolution are proposed which are then analyzed for a series of cases with various $\mathbf{f_c}$ and $\mathbf{A_f}$ parameters to reveal the energy evolution in focused wave generation. Section 5 summarizes the main findings of this study. Appendix A and B provide additional figures for wave flap motions and the evolutions of energy in different categories.

2. Numerical wave tank

To numerically generate focused waves, a rectangular wave tank is built based on the fully nonlinear potential theory (FNPT), as shown in Fig. 1. One flap maker is arranged at the left boundary and a damping zone is set at right hand side to reduce reflection waves from the end wall. A series of numerical probes are allocated along the tank, for recording wave free surfaces at different positions.

2.1. Mathematical theory

According to the potential wave theory with rotation, viscosity and surface tension neglected, a potential function ϕ exists and satisfies the Laplace equation and the corresponding boundary conditions as follows

$$\nabla^2\phi = 0 \tag{1}$$

$$\frac{Dx}{Dt} = \frac{\partial\phi}{\partial x}, \frac{Dy}{Dt} = \frac{\partial\phi}{\partial y}, \frac{Dz}{Dt} = \frac{\partial\phi}{\partial z} \tag{2}$$

$$\frac{D\phi}{Dt} = -\mathbf{g}z + \frac{1}{2}|\nabla\phi|^2 \tag{3}$$

$$\frac{\partial\phi}{\partial\mathbf{n}} = \mathbf{n}\cdot\mathbf{U}(t) \tag{4}$$

Eqs. (2) and (3) are the kinematic and dynamic boundary conditions respectively on the free surface in the Lagrangian form with $\frac{D}{Dt}$ denoting the total time derivative, and **g** being the gravitational acceleration; Eq. (4) is for the rigid boundaries including wave maker flap, side and bottom walls of the tank, where **U**(t) is the velocity of the corresponding boundary, and **n** is the unit normal vector pointing out of the tank boundaries. For the wave generator, as described in Eq. (4), the Neumann boundary specifying the gradient of the velocity potential is adopted as recommended in Wang et al (Wang et al., 2019). when comparing with the relaxation method. It should be noted that different from the wave generator condition adopted in this study, Wang et al. (2019). used wave inlet condition instead.

For reflection wave absorption, a combination of the Sommerfeld condition and the damping zone (Xu et al., 2022) is employed at the far end of the numerical tank, written as

$$\frac{\partial\phi}{\partial t} + \mathbf{c}\frac{\partial\phi}{\partial\mathbf{n}} = 0 \tag{5}$$

$$\frac{D\phi}{Dt} = -\mathbf{g}z + \frac{1}{2}|\nabla\phi|^2 - \nu(x)|\phi|s\mathrm{sign}\left(\frac{\partial\phi}{\partial\mathbf{n}}\right) \tag{6}$$

where **c** is the phase velocity of the characteristic wave, ν(x) is the damping coefficient.

2.2. Numerical method

The potential function ϕ in above Equations are solved by the QALE-FEM which is briefly introduced in this section and more details can be found in (Yan and Ma, 2010, Ma et al., 2001). A time step marching procedure is utilized in solving the discretized equation. Since the values of the potential function used on the free surface is either initially specified or obtained by integrating Eqs. (2) and (3) according to the results of the previous time step, the kinematic and dynamic conditions on the free surface can be changed to a Dirichlet condition as

$$\phi = \phi_f \tag{7}$$

Therefore, the potential function can be calculated by solving the mixed boundary value problem (MBVP), defined by Eqs. (1), (4) and (7), using finite element method.

The fluid domain is discretized into tetrahedral elements, and the potential function is expressed as

$$\phi = \sum_J \phi_J N_J(x,y,z) \tag{8}$$

where ϕ_J is the value of potential function at node J, and $N_J(x,y,z)$is the shape function. Using the Galerkin method, the Laplace equation and the boundary conditions can be expressed as

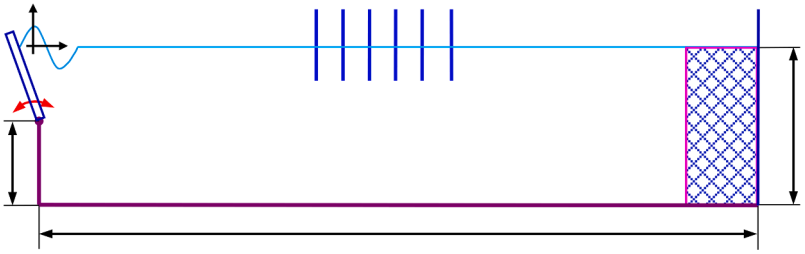

Fig. 1. Sketch of numerical wave tank.

$$\int\int\int_{\forall} \nabla N_I \cdot \sum_{J\notin S_P} \phi_J \nabla N_J d\forall = \int\int_{S_n} N_I f_n dS - \int\int\int_{\forall} \nabla N_I \cdot \sum_{\substack{J \\ J\in S_P}} (f_p)_J \nabla N_J d\forall \quad (I \notin S_P) \tag{9}$$

in which, $\mathbf{S_p}$ and $\mathbf{S_n}$ respectively represent the Dirichlet and the Neumann boundary with the potential function $\mathbf{f_p}$ and its normal derivative $\mathbf{f_n}$ treated as known values according to the results obtained in the last time step. The Eq. (9) is then written as

$$[\mathbf{A}]\{\phi\} = [\mathbf{B}] \tag{10}$$

where **B** is an array calculated from the RHS of Eq. (9) and A is a matrix discretizing the LFS of the Eq. (9). The algebraic system of Eq. (10) is solved by using a conjugate gradient iterative scheme with symmetric successive over-relaxation SSOR pre-conditioner (Ma et al., 2001).

Once the potential function is solved, the fluid velocity field can be obtained by calculating the gradient of the potential ϕ using the modified simplified finite difference interpolation method (MSFDI) (Xu et al., 2015). Comparing to the original gradient calculation scheme adopted in the QALE-FEM, MSFDI achieves higher efficiency by maintaining similar accuracy and convergent rate.

So far, the QALE-FEM has been extended to various applications, such as the 3D overturning waves with jets (Yan and Ma, 2010), multiple 3D floating bodies with 6-DoFs responses to steep waves (Ma and Yan, 2009), and is also coupled with models for solving viscous flows (Yu et al., 2022). It is employed here for the focused wave generation with the flow chart of the simulation as shown in Fig. 2.

3. Focused wave generation and validation

To generate desired focused waves, a numerical wave tank is set up as shown in Fig. 1 with water depth **d** of 3.5 m. The length of the tank **L** is 200 m and 560 m, respectively for experimental cases and other cases for further analyses, which ensure the recorded wave surfaces are not affected by reflected waves. The vertical distance from the mean free surface to the rotating axis of the wave flap is 1.86 m.

3.1. Focused wave generation

In this paper, focused waves are simulated by the phase modulation method based on the spatio-temporal focusing mechanism (Baldock et al., 1996). The wave free surface is written as

$$\zeta(x,y,t) = \sum_{n=1}^{N} a_n \cos\left[k_n(x-x_f) - 2\pi f_n(t-t_f)\right] \tag{11}$$

in which **N** is the total number of wave components, $\mathbf{x_f}$ and $\mathbf{t_f}$ are initially assigned focusing position and time, $\mathbf{a_n}$, $\mathbf{k_n}$ and $\mathbf{f_n}$ are amplitude, the wave number and wave frequency for the n^{th} wave component respectively. $\mathbf{a_n}$ is specified by the three wave amplitude distributions (spectra), as illustrated in Fig. 3.

One amplitude distribution is the Large Wave Amplitude at Low frequency (LWAL) (Xu et al., 2022), and the amplitudes of its wave components are calculated by

$$a_n = \frac{A_f}{k_n \sum_{n=1}^{N} 1/k_n} \tag{12}$$

The other two distributions are known as the Constant Wave Amplitude (CWA) (Baldock et al., 1996) and the Large Wave Amplitude at High frequency (LWAH) (Xu et al., 2022). Their $\mathbf{a_n}$ values are respectively calculated by

$$a_n = \frac{A_f}{N} \tag{13}$$

$$a_n = \frac{A_f}{k_{N-n+1} \sum_{n=1}^{N} 1/k_n} \tag{14}$$

Apart from the constant amplitude distribution of the CWA, the LWAL and the LWAH present opposite trends of the amplitudes across the frequency range. $\mathbf{k_n}$ and $\mathbf{f_n}$ are correlated in the form of $(\mathbf{2\pi f_n})^2 = \mathbf{g k_n \bullet \tanh(k_n d)}$ with $\mathbf{f_n}$ linearly increased over the specified frequency range of $\mathbf{[f_1\ f_N]}$. According to the linear wave superposition principle (Xu et al., 2019), the generated focused wave crest elevation is expected to be $\mathbf{A_f} = \sum \mathbf{a_n}$. The wave is generated by the flaps at the end of the tank and the rotation angle of the wave flap is written as

$$\theta(t) = \sum_{n=1}^{N} \frac{a_n}{F_n} \cos\left[2\pi f_n t + \left(k_n x_f - 2\pi f_n t_f\right)\right] \tag{15}$$

where $\mathbf{F_n}$ is the transfer function between the generated wave surface elevation and the rotating angle of the flap which is expressed as

$$F_n = \frac{4\omega_n^2}{g} \frac{\cosh(k_n d)[\cosh(k_n(d-h_0)) - \cosh(k_n d) + k_n d \sin(k_n d)]}{k_n^2(2k_n d + \sinh(2k_n d))} \tag{16}$$

where $\mathbf{h_0}$ is the distance from the rotating axis of wave flap to the bottom of wave tank, which is 1.64m in this wave tank. The position and the velocity of the wave flap can be calculated at each time step used as the boundary conditions at the left end of the numerical wave tank.

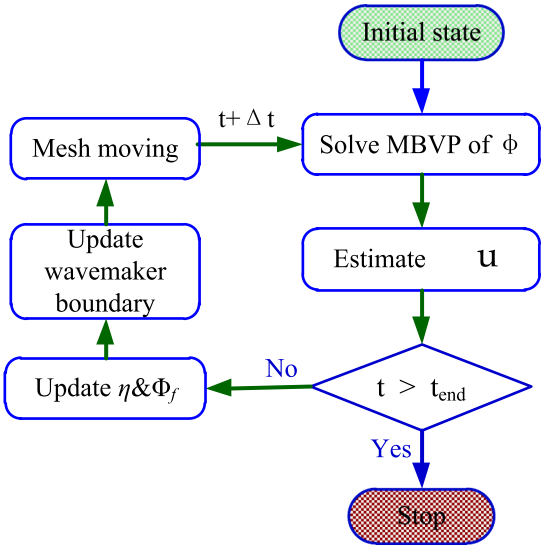

Fig. 2. Flow chart for focused wave simulation using QALE-FEM.

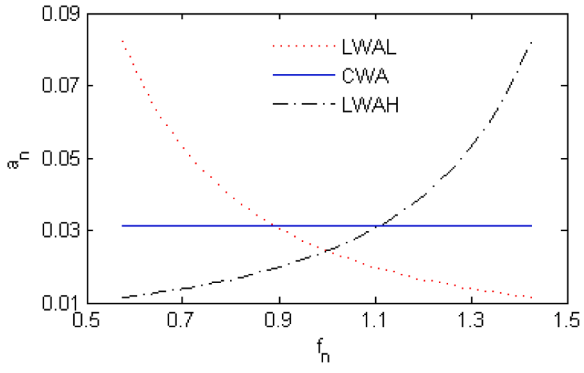

Fig. 3. Three wave component amplitude distributions over component frequencies.

It should be noted that, the effect of the nonlinear self-focusing of all the designed cases are evaluated by the Benjamin-Feir Index (BFI) proposed by Serio et al (Serio et al., 2005). It is found that all BFI values of cases are far smaller than one (Xu et al., 2022), indicating that the focused waves investigated in this research are dominated by the spatio-temporal focusing of wave energy as expressed by Eq. (11).

3.2. Validation

According to the convergence tests of this numerical wave tank carried out in (Xu et al., 2022), the results are convergent when time step reaches 1/100 of the smallest period among the wave components ($\mathbf{T_m}$) and mesh size reaches 1/20 of the corresponding wave length ($\boldsymbol{\lambda_m}$). For brevity, the detailed results of these tests are not provided here. In this work $\mathbf{T_m}/200$ and $\boldsymbol{\lambda_m}/35$ are chosen for all the tests if not stated otherwise.

A series of tests were conducted for focused wave simulation validation against experimental data (Xu, 2016). 24 wave probes were arranged along the length of the physical wave tank with the far left one arranged at 21.905 m, 31.495 m and 38.905 m from the wave maker when $\mathbf{x_f}$ is specified as 30 m, 40 m and 50 m respectively. Such shifting of the wave probes is to precisely capture the wave crests for waves focus at different locations. The distance between two neighboring probes is 0.40 m. The comparisons of spatial and temporal variations of the wave surface between numerical results and measured data for $\mathbf{A_f} = 0.1$ m, $\mathbf{f_n} = 0.1694$–0.4546 Hz, $\mathbf{x_f} = 30$ m, $\mathbf{t_f} = 36$ s and $\mathbf{N} = 32$, are demonstrated in Fig. 4.

The development and decay of the focused wave surface over 10 s at $\mathbf{x} = 23.505$ m obtained from the numerical wave tank agree well with those measured in the physical wave tank as illustrated in Fig. 4(a). The relative error of the maximum wave crest elevation is about 1 %. For all other validation cases with $\mathbf{A_f}$ varying from 0.10 m to 0.20 m and a series of frequency ranges between 0.5882 Hz and 0.1250 Hz, the maximum error of focused wave crest elevations is approximately 5 %. Due to limited number of wave gauges distributed along the physical wave tank, only a small section of space wave surface is captured by the experiments at focusing time as plotted in Fig. 4(b). The numerical results spanning over 10 m along the tank at $\mathbf{t} = 34.66$ s also agrees well with the measurements with the deviation of the focused position smaller than 1 % for this case. For all other spatial comparisons, the error of focusing positions predicted is smaller than 6 %. More detailed validation results can be found in Xu (2016).

4. Results and Discussion

For all the following test cases, the assigned focusing time $\mathbf{t_f}$, focusing position $\mathbf{x_f}$ and number of wave components $\mathbf{N}$ are set as 36 s, 50 m and 32, respectively, unless otherwise stated. 601 wave probes with the interval of 0.1 m are arranged in the vicinity of $\mathbf{x_f}$ from 20.0 m to 80.0 m for investigating wave energy variations across the frequency band of the focused wave generated. The total energy is divided into three parts, namely lower-frequency energy, wave-frequency energy and higher-frequency energy, corresponding to three frequency intervals of $\mathbf{f_n} < \mathbf{f_1}$, $[\mathbf{f_1}\ \mathbf{f_N}]$ and $\mathbf{f_n} > \mathbf{f_N}$. The wave-frequency energy is that of the components fall in the originally specified frequency range, and the other two are those of the components out of the specified frequency range, either higher than f_N or lower than f_1, produced in the process of focused wave generation. Neither the lower-frequency nor the higher-frequency energy are desired because they can distort tailored focused wave results (Xu et al., 2022) or induce extra erroneous responses of the tested floating structures, such as exaggerated slow drift or higher frequency resonance (Xu, 2016).

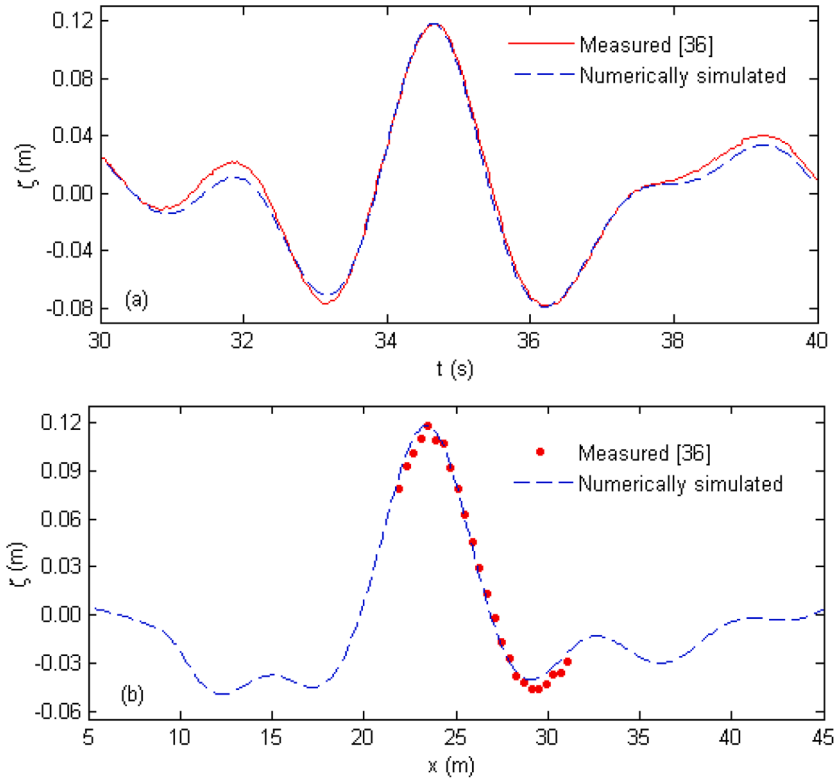

Fig. 4. Comparisons of focused wave surfaces between numerical and experimental results: (a) time history of the focused wave surface at the actual generation position ($\mathbf{x} = 23.505$ m); (b) focused wave surface profiles at the actual generation time ($\mathbf{t} = 34.66$ s).

To quantitatively assess amount and distribution of energies in three groups, four indicators are defined and formulated as follows

$$C_{EL} = \frac{\int_0^{f_1} S(f)df}{\int_{f_1}^{f_N} S_0(f)df} \tag{17}$$

$$C_{EW} = \frac{\int_{f_1}^{f_N} S(f)df}{\int_{f_1}^{f_N} S_0(f)df} \tag{18}$$

$$C_{EC} = \frac{\int_{f_1}^{f_N} S(f)\cdot fdf}{\int_{f_1}^{f_N} S(f)df} \cdot \frac{\int_{f_1}^{f_N} S_0(f)df}{\int_{f_1}^{f_N} S_0(f)\cdot fdf} \tag{19}$$

$$C_{EH} = \frac{\int_{f_N}^{\infty} S(f)df}{\int_{f1}^{f_N} S_0(f)df} \tag{20}$$

where $\mathbf{C_{EL}}$, $\mathbf{C_{EW}}$ and $\mathbf{C_{EH}}$ are energies in lower, initial and higher frequency bands respectively which are all normalized by the energy initially specified at wave-frequency interval. $\mathbf{C_{EC}}$ is the centroid of energy spectrum falling in the initial frequency band, which is used to describe the alternation of the energy distribution from the initial design. $\mathbf{C_{EC}}$ may be larger or smaller than one, respectively representing that the energy of the generated wave is more distributed to higher- or lower-frequency part comparing to the initial frequency interval. In Eqs. (17)–(20), $\mathbf{S(f)}$ is the energy spectrum for the generated wave at any position of the wave tank and can be acquired by the time history of wave free surface recorded using Fast Fourier Transform, while $\mathbf{S_0(f)}$ is the initially assigned energy spectrum.

4.1. A_f effects on spatial wave energy evolution

In this section, the wave energy distribution will be investigated with design wave crest $\mathbf{A_f}$ of 0.14 m, 0.20 m, 0.24 m and 0.28 m. The three wave amplitude spectra will be adopted as defined in Eqs. (12)–(14), i.e., LWAL, CWA and LWAH. The initial frequency band for all the spectra is specified from 0.1641 Hz to 0.4063 Hz. It should be noted that the focused wave cases employed in this research are mainly based on the waves generated in physical wave tanks and they are determined by the capacities of the wave generators and the tank sizes. When the waves are scaled up to the real sea state, the highest wave crest $\mathbf{A_f}$ of 0.28 m chosen in this study corresponds to the real wave elevation from 14 m to 22.4 m with the common scale of 50 to 80 which can cover the extreme ocean wave condition. However, most of the ocean wave energy is distributed in the frequency interval of 0.033 Hz to 0.200 Hz. To match the frequency range in the Section 4.1, i.e. 0.1641 Hz to 0.4063 Hz, to the real sea state, the scale needs to be reduced to 30 which leads to the maximum real wave elevation to 8.4m which represents the low or moderate sea states (Beaufort number 6 according to Beaufort Scale sea weather estimation (https://www.weather.gov/pqr/beaufort, 2024).

As the lower-frequency energy calculated by the fully nonlinear potential theory (FNPT) has shown in Fig. 5, the three spectra with various amplitude parameters share a similar overall trend of the lower-frequency energy evolution. It keeps increasing even when the crest appears in the range of $\mathbf{x/x_f}$ =0.8 - 0.9 and it peaks behind the designed focusing positions. The low-frequency energy finally decreases when $\mathbf{x/x_f} > 1.2$. Such spatial evolutions imply that the lower-frequency energy is mainly produced by the interaction among wave components in wave generation, rather than subharmonic waves produced by the wave flap (Sriram et al., 2015). Similar energy evolution is also found by Baldock et al. (1996) by comparing wave energy spectra of the focused wave at different positions, which were interpreted as the results of wave energy transfer between wave-frequency and lower-frequency components. Additionally, the second-order wave theory presented by Dalzell (1999) is also applied for assisting the analysis of the energy generation mechanism. Different from the significant increase of the lower-frequency energy before the wave focuses as demonstrated by the FNPT method, the second-order wave theory presents a minor increase from a relatively larger value at the location away from the focusing point to reach a similar peak as it is from the FNPT. The large gap in the lower-frequency energy generated by the two methods before the wave focus may be owing to that the second-order theory cannot fully capture the increasing wave component interactions along the process of focusing wave generation. This phenomenon is amplified by increasing the amplitude parameter and is more notable when LWAL spectrum is used. However, the similar peak from both methods infers that the lower-frequency energy of the focused waves is mainly caused by the second-order difference waves and higher orders have negligible effect, as estimated by the second-order wave theory.

For a given wave crest parameter $\mathbf{A_f}$ as shown in Fig. 5, the lower-frequency energy evolution relies on the wave amplitude spectrum. The LWAH spectrum always produces the smallest $\mathbf{C_{EL}}$, which indicates that the focused waves generated using the LWAH spectrum have the weakest interaction among wave components. For the other two spectra, their lower-frequency energy peaks remarkably higher than that produced by the LWAH spectrum, especially for the LWAL whose maximum $\mathbf{C_{EL}}$ is about four times and twice larger compared to those respectively produced by the LWAH and the CWA. The energies evaluated by the FNPT and the second-order wave theory both demonstrate that the LWAH can be selected for the applications if low lower-frequency energy is required. According to the energy calculation through the FNPT, if the LWAL spectrum has to be used to test the structure response under focused waves, locations after1.2$\mathbf{x_f}$ should be avoided where lower-frequency energy is significant.

As can be seen from Fig. 5, for all the spectra, larger wave crest parameter leads to more lower-frequency energy, e.g., $\mathbf{C_{EL}}$ is about five times higher when $\mathbf{A_f}$ is increased from 0.14 m to 0.28 m. To have an overall illustration of the lower-frequency energy variations over the $\mathbf{A_f}$ range, an indicator $\overline{C_{EL}}$, defined as, $\overline{C_{EL}} = \sum C_{EL}/N_s$ where $\mathbf{N_s}$ is the total number of positions recorded, is used for indicating mean lower-frequency energy in the vicinity of focusing point with $\mathbf{x/x_f}$ ranging from 0.4 to 1.6.

The $\overline{C_{EL}}$ curves shown in Fig. 6 suggest that for all the tested spectra, the lower-frequency wave energy positively associates with the focused wave crest parameter. It also confirms the LWAH produces the smallest lower-frequency energy and shows an almost linear increase with the $\mathbf{A_f}$ values. Whereas the LWAL and the CWA produce relatively more lower-frequency energy and both present remarkable increase especially for the LWAL spectrum, seeing the most significant rise with $\mathbf{A_f}$.

The higher-frequency energy (falling in the frequency band of $\mathbf{f > f_N}$) distribution along the wave tank is plotted in Fig. 7. According to $\mathbf{C_{EH}}$ curves predicted by the FNPT, for all the amplitude parameter $\mathbf{A_f}$, LWAL produces the largest energy in the higher-frequency interval compared to the other two spectra and presents notable periodic fluctuation. Such periodic fluctuation of the higher-frequency energy is also found by Ning et al. (2022) in the focused wave generation with the CWS spectrum (their spectrum is similar to the LWAL proposed in this paper).

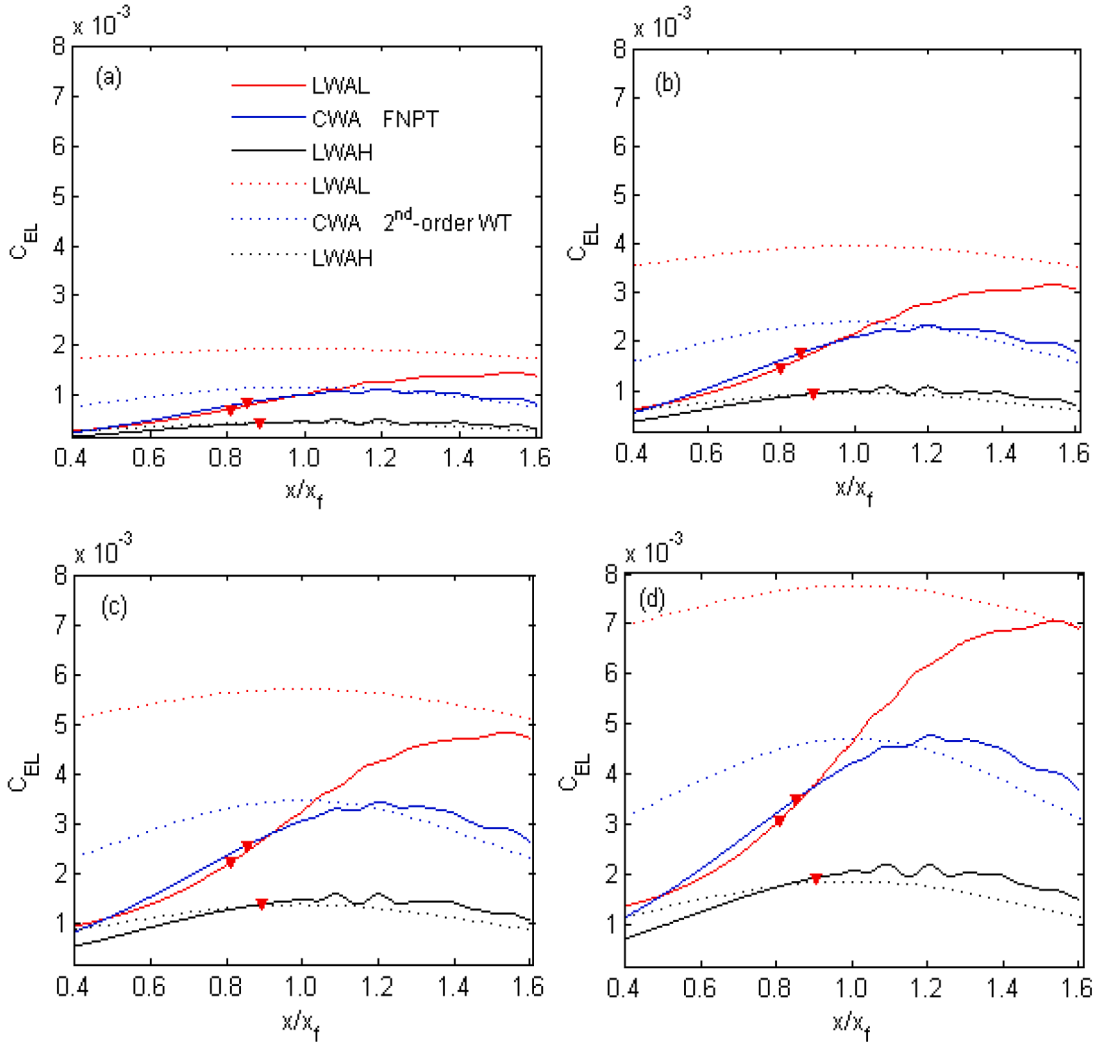

Fig. 5. Spatial variation of lower-frequency energy for three amplitude distributions with various amplitude parameters: (a) $\mathbf{A_f}$ =0.14 m; (b) $\mathbf{A_f}$ =0.20 m; (c) $\mathbf{A_f}$ =0.24 m; (d) $\mathbf{A_f}$ =0.28 m. Triangles indicate the actual focusing position of the generated wave; the solid line and the dot line in same color are respectively for the fully nonlinear wave theory (FNPT) and the second order wave theory (2nd-order WT).

According to their investigations, the higher-frequency energy fluctuation may be caused by the energy transfer between the higher-frequency region and the initially assigned frequency region. On the contrast, the higher-frequency energy produced by the LWAH keeps the smallest and it shows slight variation when $\mathbf{x}$ is smaller than $1.2\mathbf{x_f}$, whereas it goes up when $\mathbf{x}/\mathbf{x_f} > 1.2$. Thus, the higher-frequency energy is strongly associated with the assigned wave amplitude spectra.

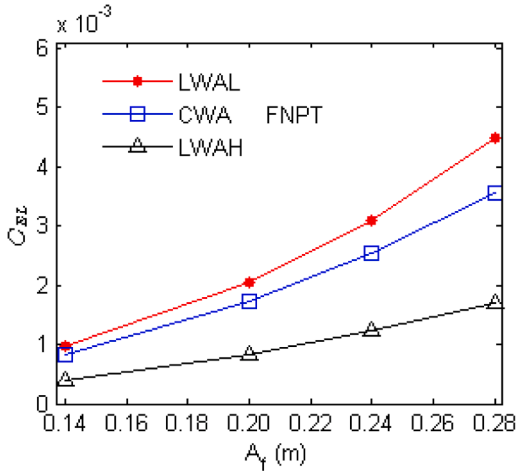

Fig. 6. Spatially averaged lower-frequency wave energy under different $\mathbf{A_f}$ values for LWAL, CWA and LWAH spectra.

In the second-order wave theory, the sum-frequency waves and the second-order Stokes components are believed to dominate the higher-frequency energy (Dalzell, 1999). However, as illustrated by the dot curves in Fig. 7, the higher-frequency energies estimated by the second-order wave theory are much smaller than those estimated by the FNPT. Furthermore, by separating the energy from FNPT into the mean value and the fluctuation, the former dominates the higher-frequency energy. It can be inferred that when using the wave maker to generate focused waves, the higher-frequency wave energy is mainly produced by the wave maker which exists across the wave tank. The larger higher-frequency energy compared to the second-order solution may be attributed to the transfer function in the adopted wave maker theory which is valid for small amplitude motions (Sriram et al., 2015; Schaffer, 1996) but may generate extra energy for larger-amplitude motions as in this study. The wave maker induced higher-frequency energy is further analyzed through wave flap movements as demonstrated in Appendix A. It shows that the larger displacement leads to more higher-frequency energy which is consistent with the trend by increasing the amplitude parameter as shown from Fig. 7 (a) to (d). Furthermore, for the same

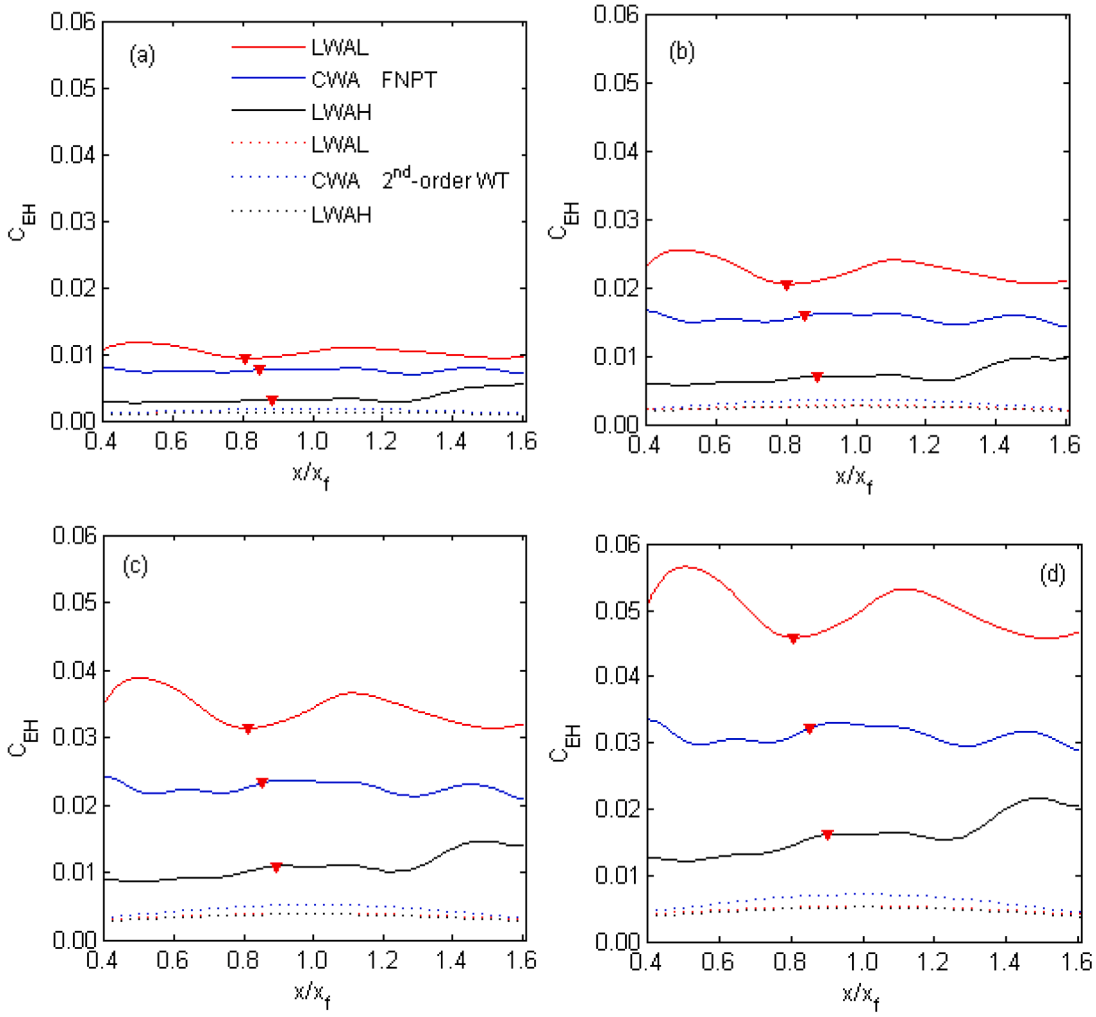

Fig. 7. Spatial variation of higher-frequency energy for three amplitude distributions with various amplitude parameters: (a) $\mathbf{A_f} = 0.14$ m; (b) $\mathbf{A_f} = 0.20$ m; (c) $\mathbf{A_f} = 0.24$ m; (d) $\mathbf{A_f} = 0.28$ m. Triangles indicate the actual focusing position of the generated wave; the solid line and the dot line in same color are respectively for the fully nonlinear wave theory (FNPT) and the second-order wave theory (2^{nd}-order WT).

amplitude parameter, the LWAL spectrum produced the largest higher-frequency energy as the displacement of the flap is larger than those of other spectra. As for the higher fluctuations over the mean value produced by the FNPT, it illustrates that the sum-frequency waves from the linear and the second-order effects play limited role on the higher-frequency energy while the nonlinear interaction among wave components which are higher than second-order such as phase coupling (Abroug et al., 2020; Deng et al., 2016) is dominant.

The spatially averaged higher-frequency wave energy, $\overline{C_{EH}}$, varying under different wave crest parameters is also calculated in the same way as that for the lower-frequency energy and is shown in Fig. 8. Similar trends can be found as those for the lower-frequency energy that the energy is positively correlated to the amplitude parameter $\mathbf{A_f}$, but the energy in the higher-frequency interval is one order of magnitude higher than that in the lower-frequency interval as predicted by the FNPT. Taking the example of the case with $\mathbf{A_f}$ of 0.28 m under the LWAL spectrum, its $\mathbf{C_{EH}}$ solved by the FNPT is about 5×10^{-2}, while its $\mathbf{C_{EL}}$ is only around 7×10^{-3}. Moreover, the higher-frequency energy is also the lowest from the LWAH spectrum and the highest from the LWAL.

In this section, the wave-frequency energy indicated by $\mathbf{C_{EW}}$ is shown in Fig. 9. It can be seen that results from FNPT deviate from 1.0 showing that the energy in the initially assigned frequency interval is not maintained. It either increases when $\mathbf{C_{EW}} > 1$ or decreases when $\mathbf{C_{EW}} < 1$. According to the $\mathbf{C_{EW}}$ obtained by the second-order theory which is well

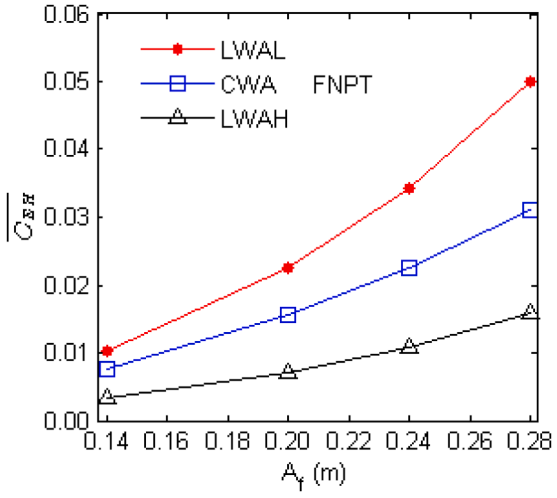

Fig. 8. Spatially averaged higher-frequency wave energy under different $\mathbf{A_f}$ parameters for LWAL, CWA and LWAH spectra.

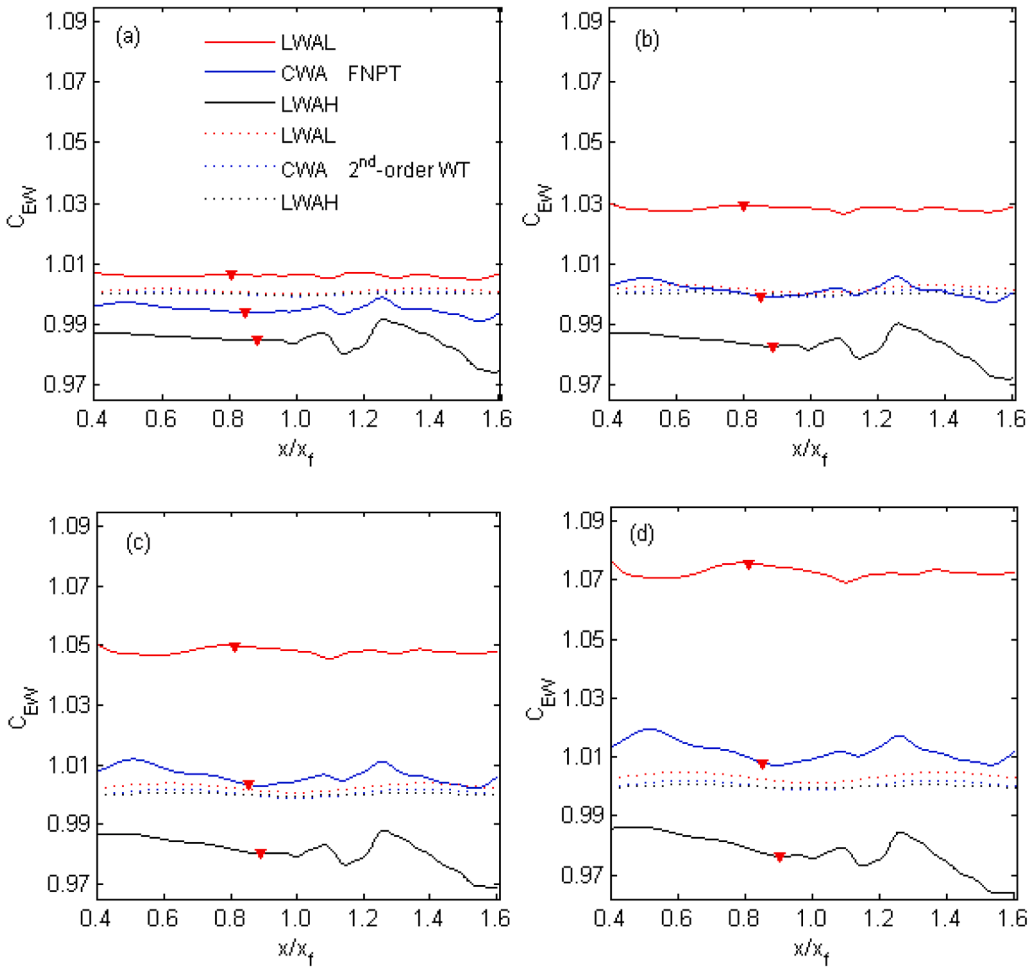

Fig. 9. Spatial variation of wave-frequency energy for three amplitude distributions with various amplitude parameters: (a) $\mathbf{A_f}$ =0.14 m; (b) $\mathbf{A_f}$ =0.20 m; (c) $\mathbf{A_f}$ =0.24 m; (d) $\mathbf{A_f}$ =0.28 m. Triangles indicate the actual focusing position of the generated wave; the solid line and the dot line in same color are respectively for the fully nonlinear wave theory (FNPT) and the second-order wave theory (2nd-order WT).

remained at 1 regardless the change of amplitude parameter and the spectrum, it indicates the effects from second-order wave, i.e. the sum-frequency waves and the second-order Stokes components within the wave-frequency interval, on the wave-frequency energy discrepancies are negligible. Furthermore, the wave-frequency energy from the LWAL is slightly larger than the assigned one and the spatial variation of the energy in the wave flume is moderate. For CWA and LWAH, the energies are almost maintained as initially assigned with slight variation especially before the positions where the focused wave occur, i.e. $\mathbf{x} / \mathbf{x_f} < 1.0$. For focused waves with larger crest elevation, the wave-frequency energy is also amplified due to the use of wave maker theory for large motion of the wave flap as discussed for Fig. 7.

Apart from the amount of energy generated within the initially assigned frequency range indicated by $\mathbf{C_{EW}}$, the distribution of the energy in this interval quantified by $\mathbf{C_{EC}}$ in Eq. (19) is also analyzed to reveal the spatial deviation of the energy distribution from the initial design. As shown in Fig. 10 the distribution of the wave-frequency energy close to the focusing points is clearly altered at most positions although the total energy only has a small fluctuation as shown in Fig. 9. Throughout the wave tank, the $\mathbf{C_{EC}}$ curves periodically fluctuate around 1.0 which stands for exact the same energy distribution as initially assigned. This implies that even for the energy falling within the initial frequency interval, it is always redistributed and tends to allocate more energy to higher ($\mathbf{C_{EC}} > 1$) or lower ($\mathbf{C_{EC}} < 1$) frequency part of the assigned interval. Similar changes of the wave-frequency energy are also noted by Liu and Mori (2000) on focused waves. Only at limited positions, the assigned energy distribution is little changed, e.g., when x is equal to $\mathbf{x_f}$ for the cases using the CWA spectrum as demonstrated by FNPT method. For the studies requiring accurate wave energy distribution over the assigned interval, such as RAOs experiment of floating body (Takezawa and Hirayama, 1976), the testing locations at wave tank need to be more carefully selected to ensure accurate responses. In addition, the more energy allocated to the high frequency within the interval may lead to nonlinear response of the floating body (Takezawa and Hirayama, 1976; Xu, 2016) and wave breaking is likely to occur prematurely during the generation process of the focused wave (Abroug et al., 2020).

As demonstrated in Fig. 10, $\mathbf{C_{EC}}$ curves evaluated by the two theories also show that the three wave amplitude spectra have different effects on the spatial wave-frequency energy distributions. The $\mathbf{C_{EC}}$ based on the LWAL has the largest fluctuation, whereas for the uniformly distributed amplitude, i.e., the CWA spectrum, its $\mathbf{C_{EC}}$ fluctuations become moderate and has similar peak and trough values. LWAH spectrum, in which large amplitudes are initially assigned to high frequency components, produces the smallest fluctuation and maintains the distribution best comparing to the other two spectra. Thus, the selected wave amplitude spectra will significantly influence the wave-frequency energy distribution in focused wave generation.

Moreover, when comparing with the $\mathbf{C_{EC}}$ curves calculated by the second-order wave theory, those predicted by the FNPT show much larger amplitudes for the cases using the LWAL and the CWA and positively deviate from the horizontal line of $\mathbf{C_{EC}} = 1$. To further analyze the

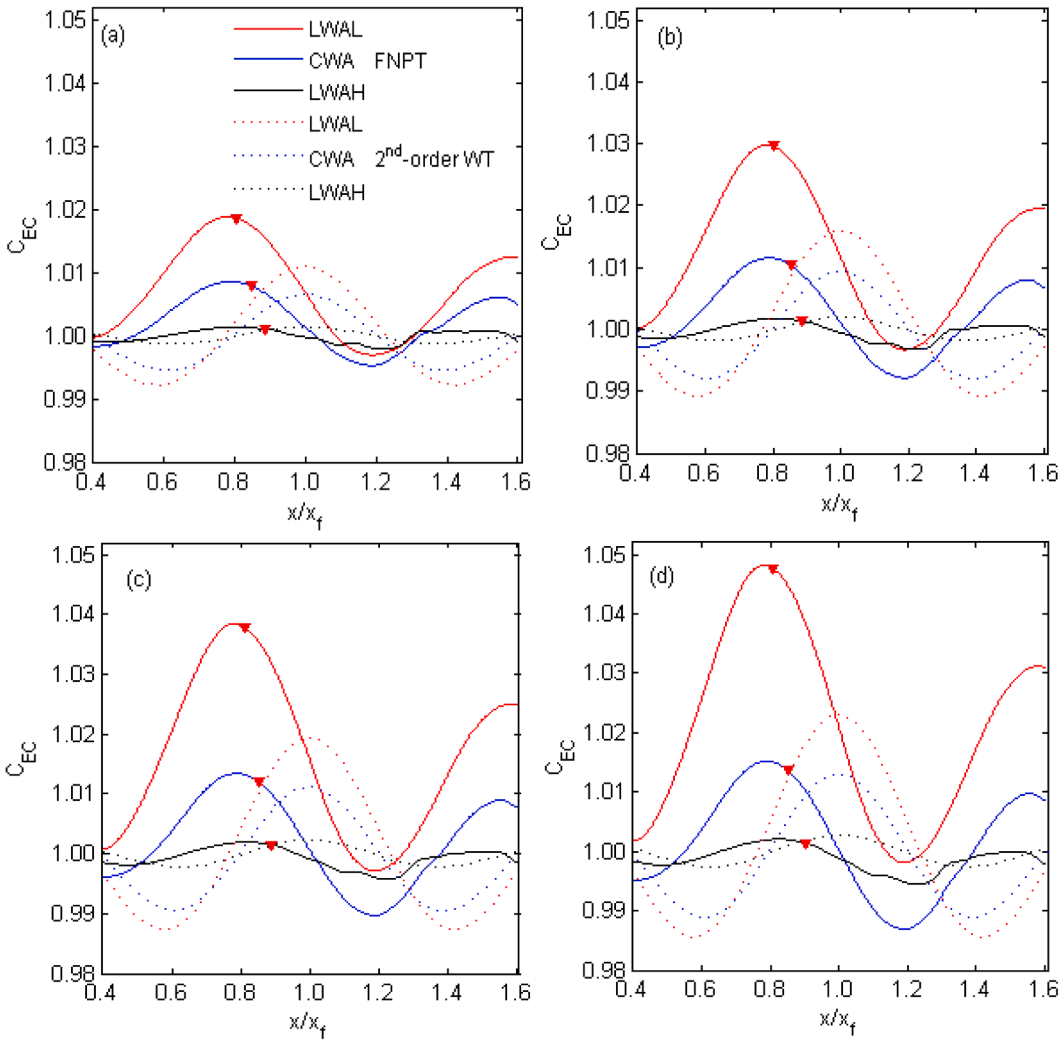

Fig. 10. Spatial variation of energy distributions being at initially assigned interval for cases with various amplitude parameters: (a) $\mathbf{A_f} = 0.14$ m; (b) $\mathbf{A_f} = 0.20$ m; (c) $\mathbf{A_f} = 0.24$ m; (d) $\mathbf{A_f} = 0.28$ m. Triangles indicate the actual focusing position of the generated wave; the solid line and the dot line in same color are respectively for the fully nonlinear wave theory (FNPT) and the second-order wave theory (2nd-order WT).

difference of the $\mathbf{C_{EC}}$ values acquired by the two theories, the amplitude spectra at positions where their $\mathbf{C_{EC}}$ maxima reach are illustrated in Fig. 11 (a) and (b), respectively for the LWAL and the CWA. The difference of $\mathbf{C_{EC}}$ values evaluated by the two methods is mainly caused by the wave components at high frequency part of $[\mathbf{f_1}\ \mathbf{f_N}]$, i.e. 0.3 Hz to $\mathbf{f_N}$ where the amplitudes calculated by the FNPT is notably higher than those from the second-order wave theory, while the components falling in the range from $\mathbf{f_1}$ to 0.3 Hz largely remain similar to the design spectra for the both methods. It implies that LWAL and CWA have strong nonlinear interaction among wave components, such as phase coupling (Deng et al., 2016), generating extra components at the higher end of the wave frequency range. For the waves based on the LWAH, the $\mathbf{C_{EC}}$ curves calculated by the two theories have similar fluctuation amplitude, which is also further verified by their amplitude spectra having good agreement as shown in Fig. 11(c).

Besides, as illustrated in Fig. 10, the focusing position is also effected by wave amplitude spectra adopted in wave generation. In general, the LWAH produces the farthest position and the LWAL occurs at nearest location. The difference of their focusing positions is mainly caused by their wave steepness which has been pointed out by both Xu et al. (2022) and Wang et al. (2019). According to analysis of wave energy evolution, the focusing position (marked as triangle in Fig. 10) is further associated with the distribution of wave-frequency energy. As the $\mathbf{C_{EC}}$ curves demonstrate, all focused waves are almost generated at the positions where the corresponding $\mathbf{C_{EC}}$ reaches the maximum. Therefore, the $\mathbf{C_{EC}}$ values may be used as an indicator for qualitatively confirming the occurrence of the focused wave in numerical or physical wave tank.

To further investigate the wave-frequency energy distribution with different $\mathbf{A_f}$ values, the mean value of each curve and the fluctuation amplitude in Fig. 10 are respectively calculated as $\overline{C_{EC}} = \sum C_{EC}/N_s$ and $\overline{H_{EC}} = (C^+_{EC} - C^-_{EC})/2$ where C^+_{EC} and C^-_{EC} are the maximum and the minimum values on each curve.

Based on the two indicators calculated by the FNPT shown in Fig. 12, they suggest that the alteration of wave-frequency energy distribution is affected by both the amplitude spectra and $\mathbf{A_f}$. The highest $\overline{C_{EC}}$ and $\overline{H_{EC}}$ curves are both from the waves generated by the LWAL which modifies the energy distribution most with the largest portion of the energy reallocated to the high frequency part of the assigned frequency interval. In addition, the increase of energy relocation is sensitive to the $\mathbf{A_f}$ increase. On the contrary, both indicators of the LWAH are the smallest and almost maintain constant with the A_f increase. Thus, it once again suggests that the originally assigned energy distribution can be better kept for the waves generated by the LWAH spectrum even though the generated focused waves crest is higher than expected as pointed out in (Xu et al., 2022).

In addition, it should be noted that the nonlinear self-focusing of the

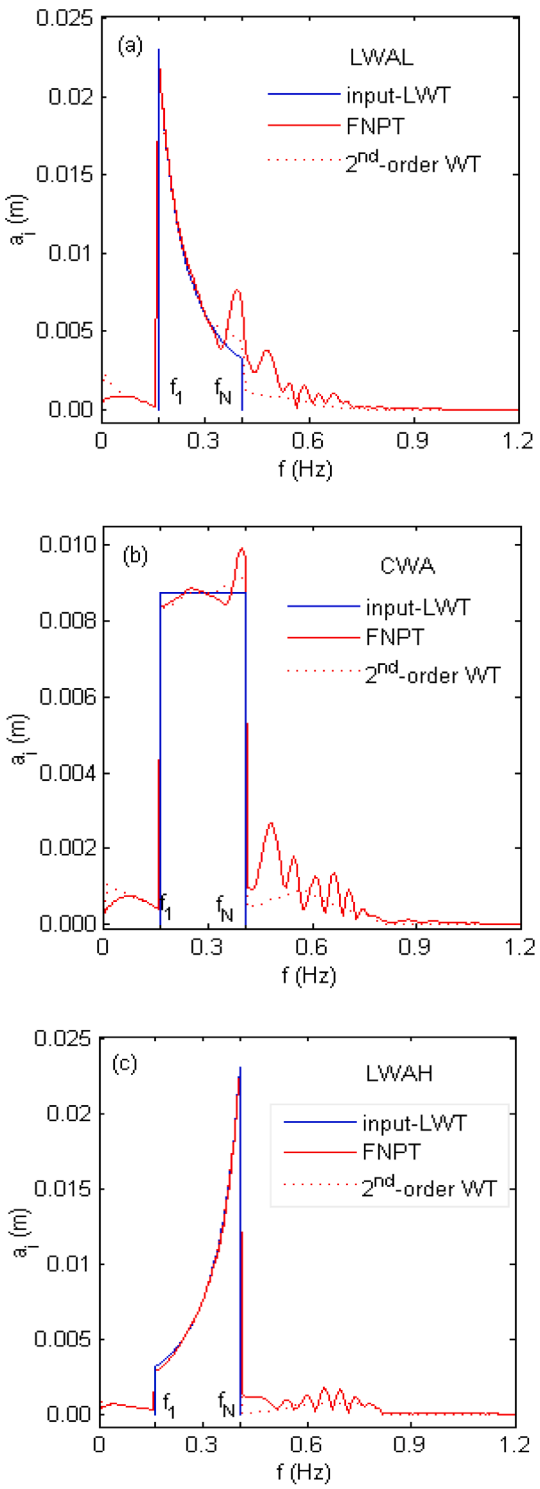

Fig. 11. Amplitude spectra generated by the FNPT in red solid line and the 2nd-order wave theory in red dash line. The blue line is the initial input spectra according to linear wave theory (LWT).

wave energy is likely to be induced for the waves with higher crests. However, the generation of focused waves here is found to be dominated by the spatio-temporal focusing of wave energy due to that the energy within the initial frequency interval is well maintained as illustrated in Fig. 9.

4.2. f_c effects on spatial wave energy evolution

This Section is to investigate the effects of different wave-frequency intervals on spatial energy evolution alongside the focused wave generation. By keeping the band width of the frequencies constant, i.e., $\Delta \mathbf{f} =$ 0.2422 Hz, the frequency intervals vary by shifting their central frequency $\mathbf{f_c}$ from 0.2461 Hz to 0.3242 Hz. For all the tested cases, the wave crest parameter $\mathbf{A_f}$ is fixed to be 0.14 m.

The spatial variation of $\mathbf{C_{EL}}$ calculated by the FNPT and the second-order wave theory for different frequency ranges are tested. As discussed in 4.1 for the amplitude effects, similar trends are obtained among wave spectra for the frequency effects. The reasons for the differences between FNPT and 2nd-order wave theory have also been discussed in 4.1. For brevity, the figures showing spatial $\mathbf{C_{EL}}$ variation for four frequency intervals are provided in Fig. B1 of Appendix B. Based on the definition for the spatially averaged energy $\overline{C_{EL}}$ proposed in the Section 4.1, Fig. 13 demonstrates that the averaged lower-frequency energy gradually decreases by shifting the frequency band to the higher end. Moreover, the LWAL spectrum always produces the largest lower-frequency energy and it is followed by the CWA and LWAH spectra. Thus, to generate the focused waves with less lower-frequency energy, the LWAH spectrum is more preferable as it can help minimize the energy transfer to the lower-frequency interval, especially for cases with frequency ranges being in the lower frequency domain.

The comparison of higher-frequency energies over different $\mathbf{f_c}$ for the three spectra is summarized by the spatially averaged energy indicator $\overline{C_{EH}}$ as shown in Fig. 14. Based on the results from the FNPT, it can be seen that the focused waves produced by the LWAL spectrum has the largest higher-frequency energy and it is almost maintained steady when the frequency range is moved towards the higher end. However, the higher-frequency energies of the other two spectra present significant decrease when $\mathbf{f_c}$ increases. The detailed spatial variations of higher-frequency energy as represented by $\mathbf{C_{EH}}$ for different frequency ranges, are provided in Fig. B2 of Appendix B as the curves for three spectra are generally similar as those for different wave crest parameters as shown in Fig. 7. With frequency band varied, the findings of the mechanism producing the higher-frequency energy for amplitude parameter variations are still valid. The higher mean energy is likely caused at the wave paddle due to the large displacement for focused wave generation while the larger variation over the mean value may be induced by the higher-order wave interaction which is not included in the 2nd-order wave theory.

For the wave-frequency energy of above cases, their spatial fluctuation is plotted in Fig. B3 of Appendix B which are also similar to those for different amplitude parameters as demonstrated in Fig. 9. The energy distributions indicated by $\mathbf{C_{EC}}$ are plotted in Fig. 15. From $\mathbf{C_{EC}}$ curves obtained by FNPT, it can be seen that the energy distributions for different wave-frequency ranges keep fluctuating along the wave tank. In general when the central frequency becomes larger, the energy distribution is better maintained. For the cases with $\mathbf{f_c}$= 0.2461 Hz, all $\mathbf{C_{EC}}$ curves have visibly larger troughs, compared with their crests, which implies that more energy trends to be distributed to low frequency components. When $\mathbf{f_c}$ is shifted to 0.3242 Hz, the $\mathbf{C_{EC}}$ curves of the three spectra all slightly deviate from 1.0. Nevertheless, comparing among the three spectra, LWAL produces the largest fluctuation of $\mathbf{C_{EC}}$ indicating the maximum energy redistribution at [$\mathbf{f_1}$ $\mathbf{f_N}$]. Overall, the difference among $\mathbf{C_{EC}}$ values is limited and is within 2 % when the frequency interval moves.

In addition, Fig. 15 also demonstrates the generation positions of the focused waves all appear around the peak of each curve. This phenomenon is consistent with that found in the tests of the wave crest parameters at Section 4.1, in which the maximum $\mathbf{C_{EC}}$ can be used to infer the focusing position.

With the frequency range shifting to the high frequency end, all the $\overline{C_{EC}}$ curves plotted in Fig. 16(a) slightly vary about 1, indicating that the

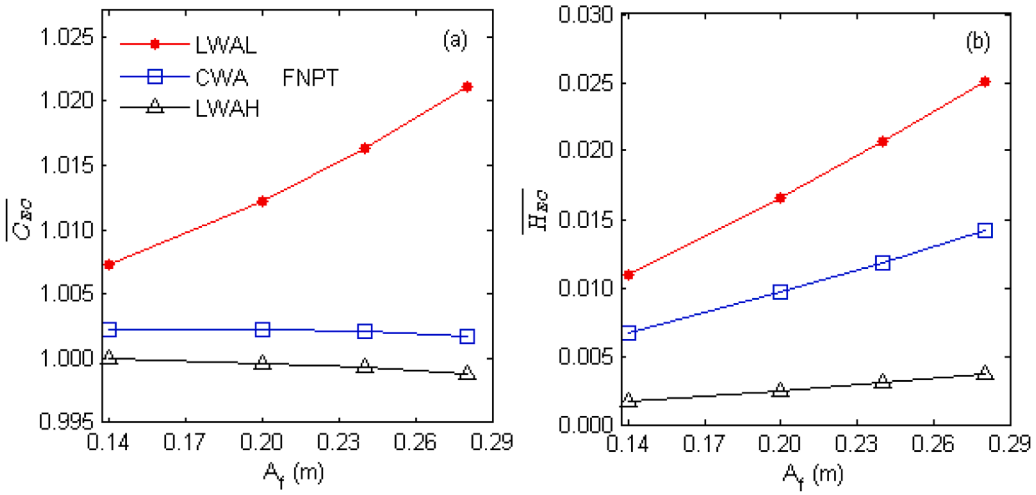

Fig. 12. Variation of wave-frequency energy distribution under different wave crests: (a) the spatially averaged value of $\mathbf{C_{EC}}$; (b) the fluctuation amplitude of $\mathbf{C_{EC}}$.

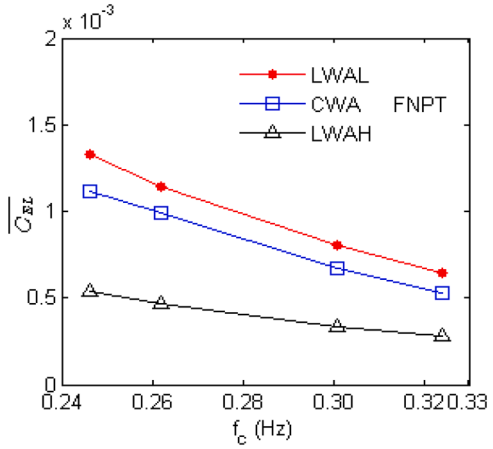

Fig. 13. Spatially averaged lower-frequency wave energy over various $\mathbf{f_c}$ values.

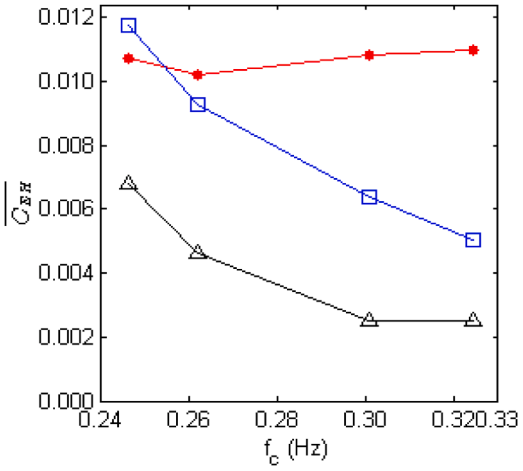

Fig. 14. Spatially averaged higher-frequency wave energy over various $\mathbf{f_c}$ values.

overall energy redistribution due to assigned frequency range shift and the wave amplitude spectra choices is limited and is less than 1 %. Moreover, the deviation of the wave energy distribution from that of the initial design gradually weakens with the increase of the frequency for all the three spectra as illustrated in Fig. 16(b). The deviation level, as indicated by $\overline{H_{EC}}$, is the lowest across the tested frequency ranges if LWAH spectrum is used. Therefore, the LWAH spectrum is able to better maintain the initially assigned energy distribution for various frequency ranges.

5. Conclusions

This research investigates spatial energy evolution of focused waves, based on the numerical results obtained from solving the fully nonlinear potential wave theory utilizing the Quasi Arbitrary Lagrangian-Eulerian-Finite Element Method (QALE-FEM). For clearly and quantitatively describing the spatial wave energy variation, four indicators, i.e., $\mathbf{C_{EL}}$, $\mathbf{C_{EH}}$, $\mathbf{C_{EW}}$ and $\mathbf{C_{EC}}$, are proposed corresponding respectively to relative energies being at the frequency intervals of $\mathbf{f} < \mathbf{f_1}$ (lower-frequency), $\mathbf{f} > \mathbf{f_N}$ (higher-frequency), and $[\mathbf{f_1}\ \mathbf{f_N}]$ (wave-frequency), and energy distribution alteration over assigned wave-frequency interval $[\mathbf{f_1}\ \mathbf{f_N}]$. The higher-, lower- and wave-frequency energies as well as the energy redistribution obtained by the fully nonlinear theory are also compared with those from the second-order wave theory for analyzing the mechanism of the energy evolution alongside the focusing wave generation. The main conclusions are given below:

The lower-frequency wave energy gradually increases at positions before $1.2\mathbf{x_f}$, and then begins to drop steadily while the higher-frequency energy shows slight fluctuations over large mean value along the tank near the focusing position. It suggests that during the early stage of the wave evolution, the lower-frequency energy is mainly generated by the interaction among wave components and the higher-frequency energy is likely produced by the wave maker. Those findings are consistent with the comparison between the FNPT and the second order-wave theory. The lower-frequency energy from the nonlinear method is lower than that from the second-order theory before the focusing point due to weaker wave-wave interactions before all the wave components focus. The similar peak value when the wave focuses for both theories suggests that the lower-frequency energy is dominated by the second-order sum-frequency waves which are accurately predicted by the second-order wave theory. The higher-frequency energy is mainly caused by the wave paddle resulting in a constant mean value along the flume which does not exist in the results from the second-order theory.

Both higher-frequency and lower-frequency energy increase with the increase the focused wave crest elevation, while they decrease with the frequency range shifting towards to the higher frequency domain. Furthermore, the amounts of two energy categories are strongly

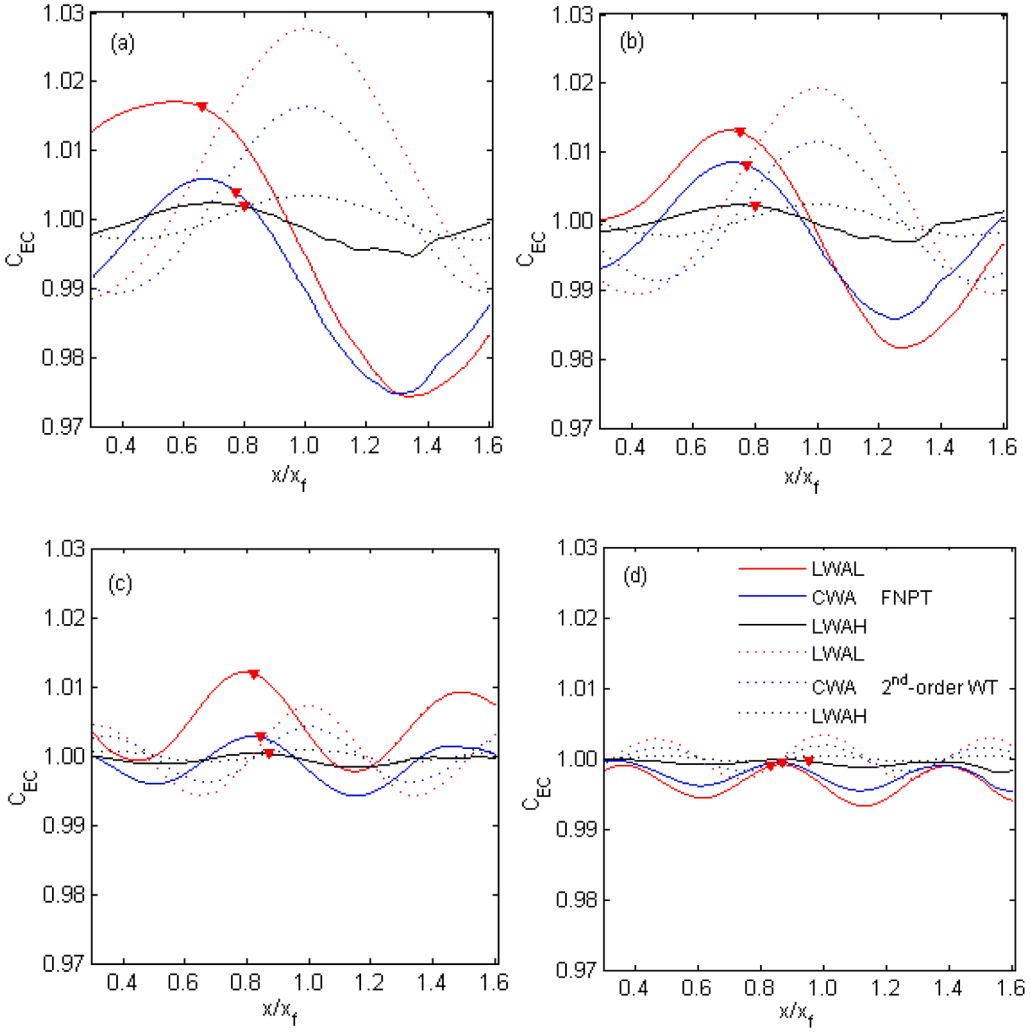

Fig. 15. Spatial variation of wave-frequency energy distribution for cases with various $\mathbf{f_c}$ parameters: (a) $\mathbf{f_c}$ = 0.2461Hz; (b) $\mathbf{f_c}$ = 0.2617 Hz; (c) $\mathbf{f_c}$ = 0.3007 Hz; (d); $\mathbf{f_c}$ =0.3242 Hz. Triangles are the focusing positions.

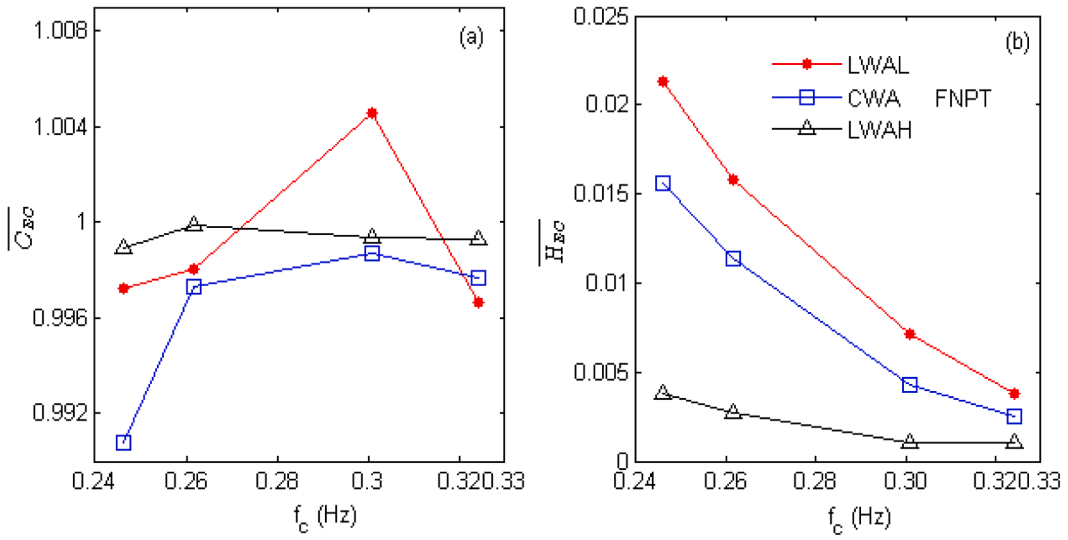

Fig. 16. variation of initially assigned wave energy distribution under different $\mathbf{f_c}$ values: (a) the mean value of $\mathbf{C_{EC}}$; (b) the fluctuation amplitude of $\mathbf{C_{EC}}$.

correlated with the initially assigned wave amplitude spectra. Specifically, more lower-frequency and higher-frequency energy will be generated if larger wave amplitudes are assigned to the low frequency components, such as the LWAL spectrum. For cases investigated in this paper, the magnitude of the lower-frequency energy is less than 1 % of that is initially assigned, whereas that in higher-frequency is one order magnitude larger than the lower-frequency one, reaching around 10 %. Although energies transferred to both frequency intervals are limited, they can disturb generation of the focused waves and may induce undesired premature breaking.

The wave-frequency energy and its distribution also rely on the assigned wave crest parameter, the frequency range and the type of initially assigned amplitude distribution spectra. The spectrum allocating larger amplitude in the lower frequency part, such as LWAL, produces more wave-frequency energy which may be even larger than the amount initially assigned. In general, the generated energy is steady along the wave tank with minor fluctuations, while its distribution presents an obvious deviation from what is designed. For the waves with higher crests and being at lower frequency domain, the deviation is more significant than those with lower crests and being at higher frequency domain due to the higher-order interactions of the wave components resulting in extra energy at the high end of the frequency interval. Comparing the three wave spectra, the waves based on the LWAH best maintain the spatial energy distribution. Although the wave-frequency energy keeps fluctuating up and down about the initial design along the wave tank, the optimum position where the wave energy distribution is best kept still exists in wave tank to be applied for RAOs tests and wave structure interaction studies.

Additionally, it is found in this study that the focused wave generation positions are associated with the distribution of the energy within the initially assigned frequency and they occur at the position where the deviation of the energy distribution reaches maximum, i.e. $\mathbf{C_{EC}}$ becomes maximum. Thus, the $\mathbf{C_{EC}}$ proposed by this research can be considered as an indicator to predict or verify focused wave generation position in numerical or physical wave tank.

Considering the limitation of the theoretical model and numerical method used, only the non-breaking waves are considered in this paper. In the future, the breaking focusing wave can be investigated by coupling QALE-FEM and OpenFOAM the latter of which is capable to deal with the local wave breaking. Alternatively, Higher-Order-Spectra (HOS) coupled with the OpenFOAM (Aliyar et al., 2022) can also be adopted in which the nonbreaking potential function is expressed by the Taylor expansion.

CRediT authorship contribution statement

Guochun Xu: Conceptualization, Methodology, Software, Writing – original draft. **Yan Zhou:** Formal analysis, Validation, Writing – review & editing. **Shiqiang Yan:** Data curation, Methodology. **Shuai Yuan:** Data curation.

Declaration of competing interest

The authors declare that they have no known competing financial interests or personal relationships that could have appeared to influence the work reported in this paper.

Data availability

Data will be made available on request.

Acknowledgments

The authors acknowledge the supports of Zhejiang Provincial Natural Science Foundation of China (Grant No. LY21E090002), National Natural Science Foundation of China (Grant No. 51909125) and Royal Society International Exchanges 2021 Cost Share (NSFC) (IEC\NSFC \211207).

Appendix. A

Figs. A1,B1,B2,B3

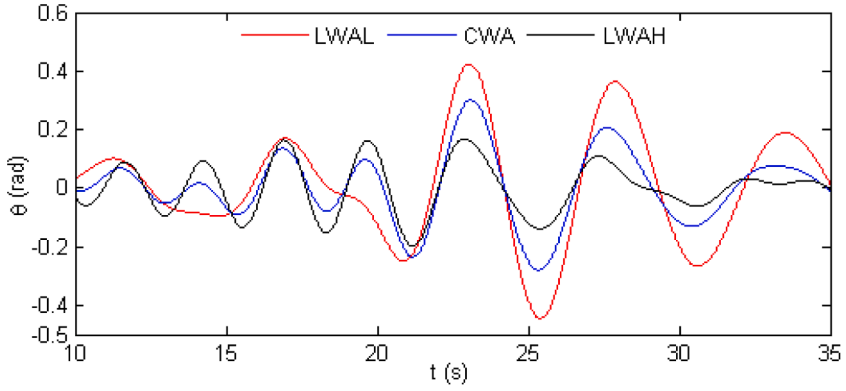

Fig. A1. Comparison of wave flap motions of the LWAL, CWA and LWAH spectra for cases with $\mathbf{A_f} = 0.28$ m.

Appendix. B

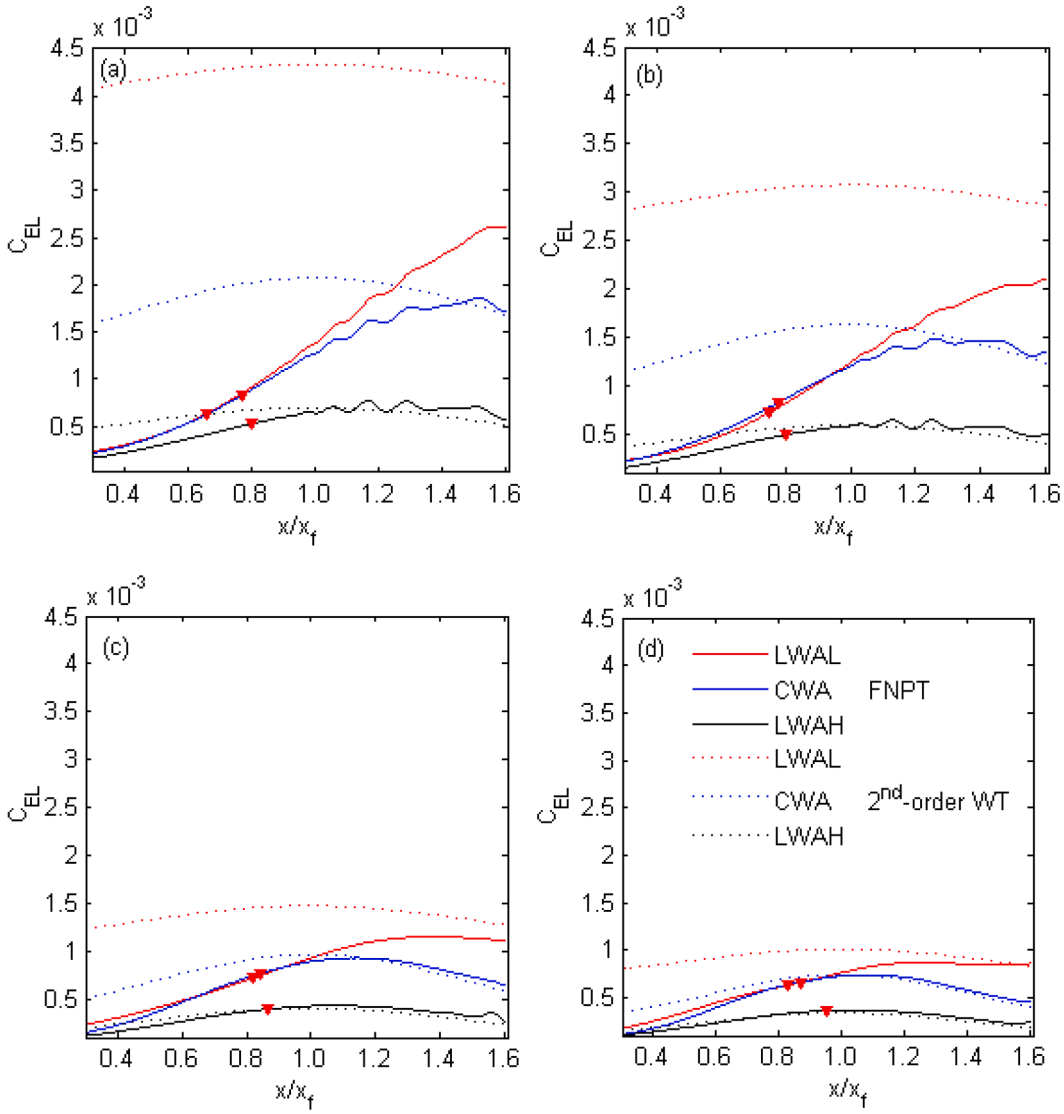

Fig. B1. Spatial variation of lower-frequency energy for focused waves: (a) $\mathbf{f_c}$ =0.2461 Hz; (b) $\mathbf{f_c}$ = 0.2617 Hz; (c) $\mathbf{f_c}$ = 0.3007 Hz; (d) $\mathbf{f_c}$ = 0.3242 Hz. Triangles indicate the actual focusing position of the generated wave; the solid line and the dot line in same color are respectively for the fully nonlinear wave theory (FNPT) and the second-order wave theory (2^{nd}-order WT).

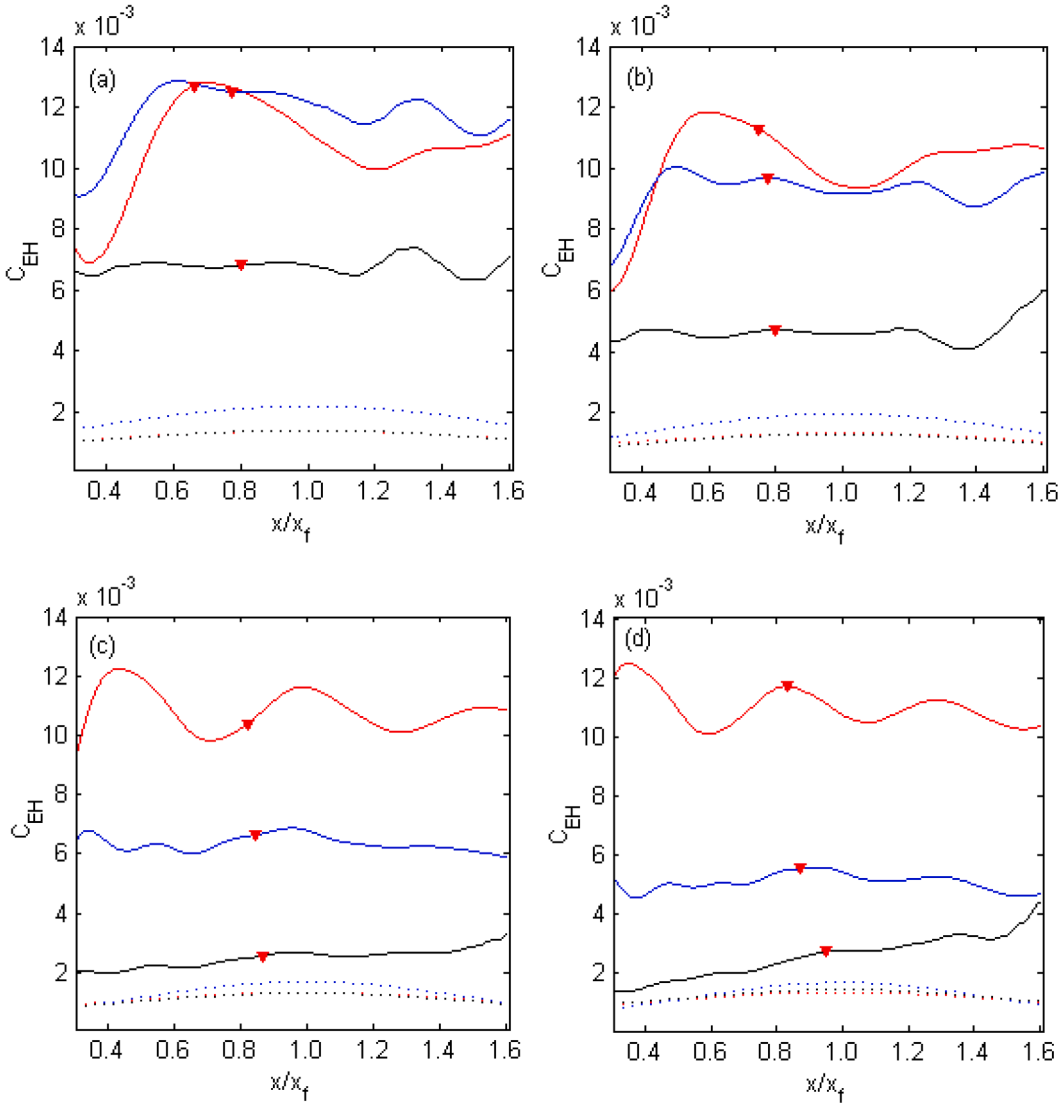

Fig. B2. Spatial variation of $\mathbf{C_{EH}}$ for focused waves under different frequency ranges: (a) $\mathbf{f_c}$ = 0.2461 Hz; (b) $\mathbf{f_c}$ = 0.2617 Hz; (c) $\mathbf{f_c}$ = 0.3007 Hz; (d) $\mathbf{f_c}$ = 3242 Hz. Triangles indicate the actual focusing position of the generated wave; the solid line and the dot line in same color are respectively for the fully nonlinear wave theory (FNPT) and the second-order wave theory (2^{nd}-order WT).

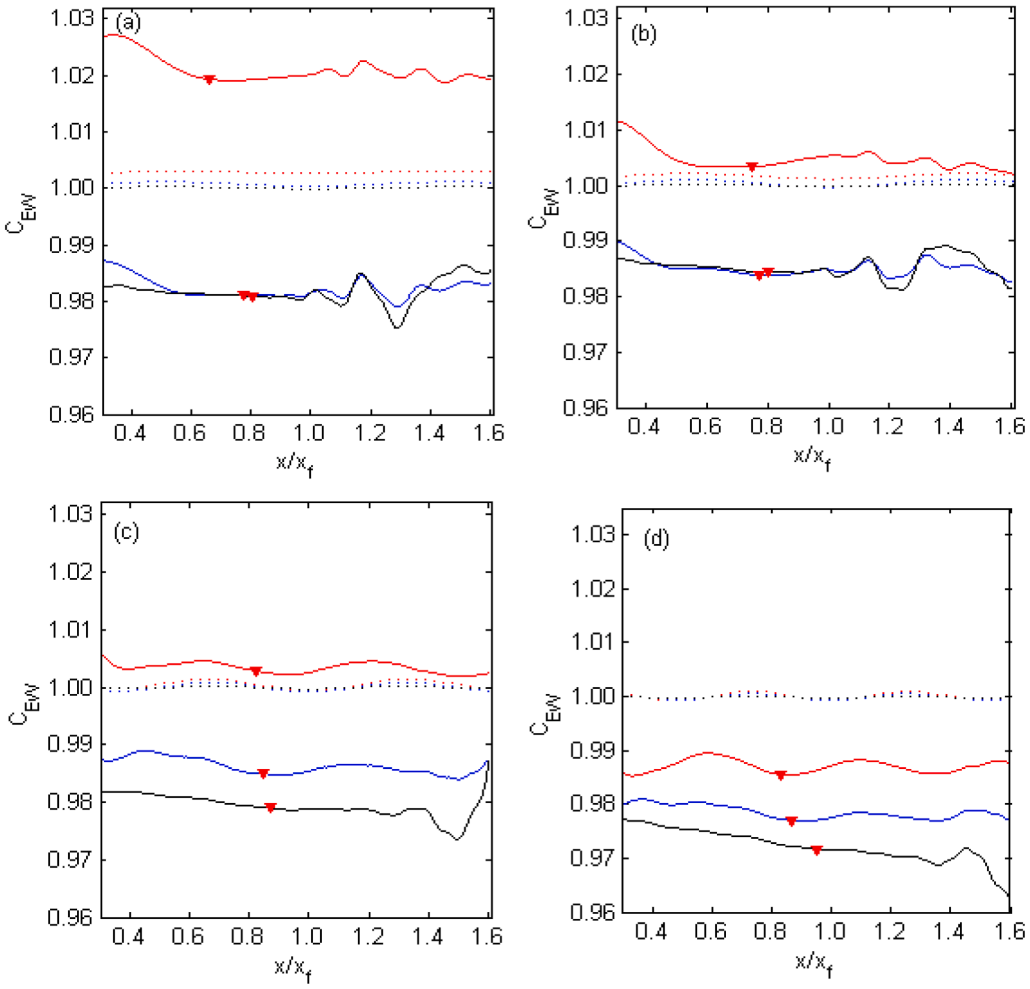

Fig. B3. Spatial variation of C_{EW} for focused waves under different frequency ranges: (a) $f_c = 0.2461$ Hz; (b) $f_c = 0.2617$ Hz; (c) $f_c = 0.3007$ Hz; (d) $f_c = 3242$ Hz. Triangles indicate the actual focusing position of the generated wave; the solid line and the dot line in same color are respectively for the fully nonlinear wave theory (FNPT) and the second-order wave theory (2^{nd}-order WT).

References

Abroug, I., Abcha, N., Jarno, A., Marin, F., 2020. Laboratory study of non-linear wave-wave interactions of extreme focused waves in the nearshore zone. Nat. Hazards Earth Syst. Sci. Discuss. 2020, 1–19.

Abroug, I., Abcha, N., Dutykh, D., Jarno, A., Marin, F., 2020. Experimental and numerical study of the propagation of focused wave groups in the nearshore zone. Phys. Lett. A 384 (6).

Ai, C., Ding, W., Jin, S., 2014. A general boundary-fitted 3D non-hydrostatic model for nonlinear focusing wave groups. Ocean Eng. 89 (0), 134–145.

Aliyar, S., Ducrozet, G., Bouscasse, B., Venkatachalam, S., Ferrant, P., 2022. Breaking focused wave interaction with cylinder using HOS-OpenFOAM coupling. In: Proceedings of the AOCEANS 2022. Chennai, Chennai, India. https://doi.org/10.1109/OCEANSChennai45887.2022.9775539.

Bai, X., Yang, C., Luo, H., 2021. Hydrodynamic performance of the floating fish cage under extreme waves. Ocean Eng. 231, 109082.

Baldock, T., Swan, C., Taylor, P., 1996. A laboratory study of nonlinear surface waves on water. Philos. Trans. R. Soc. A Math. Phys. Eng. Sci. 354, 649–676.

Chabchoub, A., Peri, R., Hoffmann, N., 2014. Dynamics of unstable stokes waves: a numerical and experimental study. In: Proceedings of the 33rd International Conference on Ocean, Offshore and Arctic Engineering. San Francisco, CA, USA, 8–13 June.

Chaplin, J.R., 1996. On frequency-focusing unidirectional waves. Int. J. Offshore Polar Eng. 6 (02), 7.

Clauss, G.F., Schmittner, C.E., Klein, M., 2006. Generation of rogue waves with predefined steepness. In: Proceedings of the 25th International Conference on Offshore Mechanics and Arctic Engineering, OMAE 2006, June 4, 2006 - June 9, 2006, Hamburg, Germany.

Clauss, G., 2005. Transient wave model testing for the evaluation of extreme motions and loads of ships and semisubmersibles. Mar. Syst. Ocean Technol. 1, 103–119.

Dalzell, J., 1999. A note on finite depth second-order wave–wave interactions[J]. Appl. Ocean Res. 21 (3), 105–111.

Davies, K., Leverette, S., Spillane, M.W., 1994. Ringing response of TLP and GBS platforms. In: Proceedings of the BOSS'94, pp. 569–585.

Dean, R.G., Dalrymple, R.A., 1991. Water Wave Mechanics for Engineers and Scientists. World Scientific Publishing Co., Singapore, pp. 41–123.

Deng, Y., Yang, J., Li, X., Xiao, L., 2015. Experimental and numerical investigation on kinematics of freak waves. In: Proceedings of the 25th International Ocean and Polar Engineering Conference. Kona, Big Island, HI, USA, 21–26 June.

Deng, Y., Yang, J., Zhao, W., Xiao, L., Li, X., 2015. An efficient focusing model of focusing wave generation considering wave reflection effects. Ocean Eng. 105, 125–135.

Deng, Y., Yang, J., Zhao, W., Li, X., Xiao, L., 2016. Freak wave forces on a vertical cylinder. Coast. Eng. 114, 9–18.

https://www.weather.gov/pqr/beaufort. 2024.

Jin, P., Zhou, B., Zhang, H., Chen, L., Zhang, L., 2019. Ringing of the roll motion of a two-dimensional barge in focused wave groups. J. Mar. Sci. Technol. 24 (4).

Khait, A., Shemer, L., 2018. Application of boundary element method for determination of the wavemaker driving signal. In: Proceedings of the ASME 2018 37th International Conference on Ocean, Offshore and Arctic Engineering.

Li, J., Liu, S., 2015. Focused wave properties based on a high order spectral method with a non-periodic boundary. China Ocean Eng. 29 (1), 1–16.

Liu, P.C., Mori, N., 2000. Wavelet spectrum of freak waves in the ocean. In: Proceedings of the ACoastal Engineering 2000 - 27th International Conference on Coastal Engineering, ICCE 2000, July 16, 2000–uly 21, 2000. Sydney, NSW, Australia.

Liu, D., 2021. Extreme wave simulation with iterative adaptive approach in numerical wave flume. China Ocean Eng. 35 (1), 61–71.

Ma, Q.W., Yan, S., 2009. QALE-FEM for numerical modelling of non-linear interaction between 3d moored floating bodies and steep waves. Int J. Numer Meth Eng. 78 (6), 713–756.

Ma, Q.W., Wu, G.X., Eatock Taylor, R., 2001. Finite element simulation of fully non-linear interaction between vertical cylinders and steep waves. part 1: methodology and numerical procedure. Int. J. Numer. Methods Fluids 36 (3), 265–285.

Ma, Y., Tai, B., Dong, G., Fu, R., Perlin, M., 2022. An experiment on reconstruction and analyses of *in-situ* measured freak waves. Ocean Eng. 244, 110312.
Ning, D., Liang, C., Chen, L., Zhang, C., 2022. Numerical investigation on the propagation and evolution of focused waves over a sloping bed. Ocean Eng. 250, 111035.
Onorato, M., Osborne, A., Serio, M., Cavaleri, L., Brandini, C., Stansberg, C., 2006. Extreme waves, modulational instability and second order theory: wave flume experiments on irregular waves. Eur. J. Mech. B Fluids 25, 586–601.
Onorato, M., Residori, S., Bortolozzo, U., Montina, A., Arecchi, F., 2013. Rogue #ntexts. Phys. Rep. 528, 47–89.
Onorato, M., Proment, D., Clauss, G., Klein, M., 2013. Rogue waves: from nonlinear schrö dinger breather solutions to sea-keeping test. PLoS One 8 (2), e54629. https://doi.org/10.1371/journal.pone.0054629.
Rameeza, M., Ranjan, B.M., 2021. Numerical Investigation of Extreme Wave Impact On Coastal Bridge Deck Using Focused Waves. Ocean Engineering, p. 234.
Rameeza, M., Ranjan, B.M., Arun, K., Hans, B., 2020. Numerical simulation and analysis of phase-focused breaking and non-breaking wave impact on a fixed offshore platform deck. J. Offshore Mech. Arct. Eng. 142 (5).
Rapp, R.J., Melville, W.K., 1990. Laboratory measurements of deep-water breaking waves. Philos. Trans. R. Soc. A 331, 735–800. Mathematical and Physical Sciences.
Riesner, M., El Moctar, O., 2021. Assessment of wave induced higher order resonant vibrations of ships at forward speed. J. Fluids Struct. 103, 103262.
Schaffer, H.A., 1996. Second-order wavemaker theory for irregular waves. Ocean Eng. 23 (1), 47 (Pergamon).
Schmittner, C., Kosleck, S., Hennig, J., 2009. A phase-amplitude iteration scheme for the optimization of deterministic wave sequences. In: Proceedings of the ASME 2009 28th International Conference on Ocean, Offshore and Arctic Engineering.
Serio M., Onorato M., Osborne A.R., Janssen P.A., 2005. On the computation of the benjamin-feir index. Il nuovo cimento C. 28(6), 893-903.
Sriram, V., Schlurmann, T., Schimmels, S., 2015. Focused wave evolution using linear and second order wavemaker theory. Appl. Ocean Res. 53, 279–296.
Takezawa, S., Hirayama, T., 1976. Advanced experimental techniques for testing ship models in transient water waves. part ii: the controlled transient water waves for using in ship motion tests. In: Proceedings of the 11th Symposium on Naval Hydrodynamics: Unsteady Hydrodynamics of Marine Vehicles, pp. 37–54.
Tian, Z., Perlin, M., Choi, W., 2011. Frequency spectra evolution of two-dimensional focusing wave groups in finite depth water. J. Fluid. Mech. 688, 169–194.
Touboul, J., Giovanangeli, J., Kharif, C., Pelinovsky, E., 2006. Freak waves under the action of wind: experiments and simulations. Eur. J. Mech. B Fluids 25, 662–676.
van Rij, J., Hsiang, Y.Y., Toan, T.T., 2021. Validation of simulated wave energy converter responses to focused waves. Proc. Inst. Civ. Eng. Eng. Comput. Mech. 174 (1).
Wang, W., Kamath, A., Pakozdi, C., Bihs, H., 2019. Investigation of focusing wave properties in a numerical wave tank with a fully nonlinear potential flow model. J. Mar. Sci. Eng.
Whittaker, C., Fitzgerald, C., Raby, A., Taylor, P., Borthwick, A., 2018. Extreme coastal responses using focused wave groups: overtopping and horizontal forces exerted on an inclined seawall. Coast. Eng. 140, 292–305.
Xu, G., Yan, S., Ma, Q.W., 2015. Modified SFDI for fully nonlinear wave simulation. CMES Comput. Model. Eng. Sci. 106 (1), 1–35.
Xu, G., Hao, H., Ma, Q., Gui, Q., 2019. An experimental study of focusing wave generation with improved wave amplitude spectra. Water 11 (12), 2521. . (Basel).
Xu, G., Zhou, Y., Yan, S., Zhang, N., 2022. Numerical investigation of wave amplitude spectra effects on focusing wave generation. Ocean Eng. 265, 112550.
Xu, G., 2016. Research on Generation of FreakWave and its Effect on Truss SPAR Motions. Harbin Engineering University, Harbin, China. Ph.D. Thesis.
Yan, S., Ma, Q.W., 2010. Numerical simulation of interaction between wind and 2D freak waves. Eur. J. Mech. B Fluids 29 (1), 18–31.
Yan, S., Ma, Q.W., 2010. QALE-FEM for modelling 3D overturning waves. Int J. Numer Meth Fl. 63 (6), 743–768.
Yu, Z., Zheng, X., Hao, H., Yan, S., Ma, Q., 2022. Numerical simulation of a floating offshore wind turbine in waves using qaleFOAM. Int. J. Offshore Polar Eng. (1), 32.
Zhang, H.D., Shi, H.D., Soares, C.G., 2019. Evolutionary properties of mechanically generated deepwater extreme waves induced by nonlinear wave focusing. Ocean Eng., p. 186.